IAEA nuclear fusion

Reduced model describing resonance overlap threshold for fast ion transport by toroidal Alfvén eigenmodes

To cite this article: R. Blyth *et al* 2026 *Nucl. Fusion* **66** 026028

OPEN ACCESS
IOP Publishing | International Atomic Energy Agency Nuclear Fusion
Nucl. Fusion 66 (2026) 026028 (23pp) https://doi.org/10.1088/1741-4326/ae2938

Reduced model describing resonance overlap threshold for fast ion transport by toroidal Alfvén eigenmodes

R. Blyth[1,*], **M. Fitzgerald**[2] **and B.N. Breizman**[3]

[1] Department of Physics, Durham University, Durham DH1 3LE, United Kingdom of Great Britain and Northern Ireland
[2] United Kingdom Atomic Energy Authority, Culham Campus, Abingdon, Oxfordshire OX14 3DB, United Kingdom of Great Britain and Northern Ireland
[3] Institute for Fusion Studies, The University of Texas, Austin, TX 78712, United States of America

E-mail: rose.blyth@durham.ac.uk

Received 4 September 2025, revised 13 November 2025
Accepted for publication 8 December 2025
Published 7 January 2026

Abstract

This work introduces a reduced model to predict the ‘resonance overlap threshold’ governing transport of fast ions (FIs) by toroidal Alfvén eigenmodes (TAEs) in tokamak plasmas. TAE-FI resonance occurs within distinct ‘resonance regions’ of particle phase space, which grow wider when the TAE mode amplitude increases. If these resonance regions are separate then FI transport is limited and localised; if multiple resonance regions overlap then large-scale stochastic transport of FIs can occur, jeopardising confinement. Predicting the resonance overlap threshold between these two scenarios is an important problem in the field of FI transport modelling. Current workflows rely on computationally expensive orbit-following codes; the new reduced resonance overlap model provides a much simpler and faster alternative, for ease of implementation in integrated models. In this paper, we apply this approach to passing particles and find good agreement with more detailed numerical modelling, including HALO code simulations. Models based on this approach could provide a useful step in increasing efficiency of predictive modelling for next-generation fusion reactors.

Keywords: fast ions, TAEs, resonance, tokamak, transport

(Some figures may appear in colour only in the online journal)

1. Introduction

Fast ion (FI) transport by toroidal Alfvén eigenmodes (TAEs) is predicted to be of great importance in future tokamaks with high rates of deuterium-tritium fusion, since plasma self-heating capability relies on good confinement of fusion-product alpha particles. In future burning plasma devices such as ITER, the FI velocity is comparable to the Alfvén velocity, creating the possibility for resonant interactions between FIs and Alfvénic modes [1]. Present day tokamaks such as MAST-U [2] typically have the capability to generate a super-Alfvénic FI population via external heating sources, thus ensuring that the FI velocity is comparable to the Alfvén velocity, and allowing for the study of resonant interactions on a smaller scale.

Most Alfvénic modes are strongly damped by the Alfvén continuum. However, toroidal effects can cause different continuum branches to intersect and couple, producing gaps in the continuum where weakly-damped discrete eigenmodes can

---

[*] Author to whom any correspondence should be addressed.

exist [3, 4]. A common example of these are the TAEs, which are predicted to be a particularly important instability in ITER [5]. These modes can be driven unstable by spatial or energy gradients in the FI population, resulting in corresponding flattening of the gradients and transport of FIs [3]. Modelling these resonant interactions and the associated FI transport is therefore an essential topic in the design of future fusion reactors.

FI transport by TAEs has been studied extensively in the literature. Typically the FIs are treated as a small population separate from the bulk thermal plasma, while the TAEs are considered as linear eigenmodes of the bulk plasma. The spatial shape of the TAE eigenfunction is determined by the bulk plasma equilibrium, and only the TAE growth rate is affected by the FIs. The simplest case is that of a single isolated TAE resonance, whose amplitude is driven to saturation by the free energy in the local spatial or energy gradients of the FI distribution function. Where multiple TAE resonances exist, the 'resonance overlap threshold' defines an important distinction between two possible regimes [6]. If the TAE amplitudes are sufficiently small and the resonances sufficiently far apart, they remain as isolated resonances, and FIs can only be transported within the vicinity of each individual resonance. If the TAE amplitudes grow sufficiently large, multiple TAE resonance regions may overlap. (Resonance overlap can also occur due to other mechanisms such as frequency chirping [7]; in this paper we focus on resonance overlap due to mode amplitude growth, assuming the mode frequencies are given by the linear dispersion relation. However, the ROM formalism could also be applied to investigate frequency chirping scenarios.) When this mode amplitude threshold for resonance overlap is exceeded, the FIs suddenly begin to exhibit stochastic behaviour, since they can be 'kicked' from one resonance region to the next [8]. Evidence of this threshold has been observed in tokamak experiments [9]. If multiple overlapping TAE resonances exist throughout the plasma, global transport and loss of FIs may result. Note that overlap may occur between multiple resonance regions of the same TAE, or between resonance regions associated with different TAEs; the stochasticity threshold behaviour applies in both cases.

Reduced models for FI transport most commonly utilise quasi-linear (QL) theory, which models the evolution of the FI distribution function via a diffusion equation in phase space. Eigenmodes are typically computed using a linear MHD solver such as MISHKA or NOVA [10, 11]. Reduced models utilising QL theory include the 'resonance-broadened QL' (RBQ) [12, 13], 'critical gradient model' (CGM) [14, 15], 'kick model' [16], and ATEP [17] approaches. The foundational assumption of all QL-based models is that the FIs exhibit stochastic behaviour. This does not occur when FIs interact with a single resonance, but two overlapping resonances are sufficient to produce stochasticity. CGMs additionally assume a large number of localised, strongly-overlapping resonances [18]. In all cases, quantifying resonance overlap is essential to determine the stochasticity regime and applicability of the FI transport models.

In this work we propose a simple reduced model, referred to as the 'resonance overlap model' (ROM), for calculating the TAE-FI resonance overlap threshold. Since resonance regions grow with increasing TAE amplitude, this threshold can be considered as a TAE amplitude threshold. This threshold has been calculated analytically under specific assumptions [6]. When analysing cases outside the applicability range of the analytical theory, or when full resonance maps are required, existing methods rely on high-performance orbit-following codes such as HALO or MEGA [19–21], as well as linear MHD codes to compute the modes. The ROM uses a highly reduced system of analytical equations to produce full resonance maps with higher computational efficiency and simpler code workflow, bypassing the need for orbit-following or linear MHD codes. The ROM equations are based on an analytical framework by Berk, Breizman and Sharapov, which describes resonant interactions between particles and TAEs via the Hamiltonian equations of motion under the guiding-centre (GC) approximation [22]. The general Hamiltonian formalism applies to any plasma equilibrium and any particle trajectories, but in this paper the calculations are presented only for the simple case of co-current passing particles. The ROM is of immediate interest for plasma scenario design, by providing rapid phase-space-dependent predictions of whether large-scale stochastic FI transport by TAEs is expected, as well as defining the applicability of QL models. It is also suitable for implementation as a sub-module in more general-purpose integrated modelling codes.

The ROM as currently formulated enables calculation of resonance overlap thresholds, expressed in terms of TAE amplitudes. However, to be fully predictive for real tokamak scenarios, it would also be necessary to calculate the TAE saturation amplitudes. Assuming TAEs stabilise rapidly at saturation amplitude, these can then be compared against estimated overlap thresholds to identify whether overlap is in fact occurring, and make predictions on FI behaviour. Various methods have been developed to estimate TAE saturation amplitudes [23–27], but including these calculations is outside the scope of this work.

In section 2, a description is given of the physics basis and model equations. In section 3, the ROM is applied to two contrasting case studies. The first case study is an analytically constructed equilibrium, designed to satisfy the modelling assumptions well, and is therefore a useful case for model benchmarking. The second case study is a MAST-U equilibrium (pulse number #47133 at 225 ms), chosen as a 'worst-case scenario', since it violates most of the modelling assumptions. The fact that the ROM performs reasonably well for both cases is a good indicator of its robustness. The ROM allows for different levels of simplification, referred to as ROM (i)–(v): these range from a more accurate version incorporatinghigh-performance code outputs (ROM (i)), to a fully reduced version constructed entirely from analytical approximations (ROM (v)). This allows the effects of each individual approximation to be quantified and compared. The key result of this paper, illustrated in figure 5, is that the ROM produces reasonably accurate predictions for resonance overlap thresholds, even when high-performance orbit-following and linear MHD codes are replaced by simple analytical approximations. Most of the approximations perform surprisingly well compared to numerical simulations, even for scenarios far outside the applicability range of the analytical theory (the MAST-U case study is chosen to illustrate this). In section 4, the ROM is benchmarked against higher-accuracy simulations carried out using HALO and MISHKA. A validation of the ROM against experimental data will be published in a future work.

2. Description of the new model

2.1. Physics background

Due to the symmetries present in a tokamak plasma equilibrium, every unperturbed particle trajectory may be uniquely defined by three constants of motion (COM), plus the sign σ which defines its direction of motion relative to the plasma current. The most common choice of variables to parametrise 3D COM space is (μ, E, P_ϕ): the particle magnetic moment, energy and toroidal canonical angular momentum respectively. Resonant interactions with modes perturb particle trajectories, or equivalently alter the particle COM (i.e. shift its position in COM space). Throughout this paper, it is assumed that μ is never altered by resonant interactions or any other effects [28, 29], which is justifiable for modes such as TAEs with frequency well below the ion cyclotron frequency. This assumption reduces the dimensionality of the problem to 2D (E, P_ϕ) COM space. As an alternative parametrisation to (E, P_ϕ), later figures are plotted in (E, R_{init}), with R_{init} denoting the particle major radial position at the point where it crosses the horizontal plane of the magnetic axis ($Z = Z_0$) on the outboard side. (Note (R, Z) are the horizontal and vertical Cartesian coordinates parametrising the poloidal plane in real space.) An alternative radial COM space variable is $\bar{r}$, defined as the average of the particle's minor radial position over its full trajectory. The Hamiltonian theory formalism (see section 2.4.2) instead uses canonical action variables $(\bar{P}_\phi, \bar{P}_\theta)$ [30].

The two main categories of unperturbed particle trajectories in a tokamak are the 'passing particles' (those which always travel in the same toroidal direction) and the 'trapped particles' (those which bounce back and forth on the tokamak outboard side, trapped in a magnetic field well). Passing particles can be further categorised as co-current ($\sigma > 0$) or counter-current ($\sigma < 0$). All three trajectory types can resonate with TAEs, but the resulting effects on FI transport depend on the density of FIs in each phase space region [3, 4, 31]. Although the Hamiltonian formalism described in sections 2.4.1–2.4.2 is a general formalism applicable to all tokamak particle and trajectories, the ROM in this paper is only applied to passing particles, since their trajectories have a simpler analytical description. This case may be mainly relevant to the plasma core region [3, 31]. An extension to the trapped particle population is a topic for a future work, which may be more relevant for modelling losses at the plasma edge, and also for devices such as JET where the FI population is mainly trapped [32].

In MHD theory, TAEs occur due to toroidal coupling of different Shear Alfvén continuum modes [3, 4]. In particular, the peak TAE location occurs at the point where two counter-propagating continuum modes match in frequency. The coupling of these two modes produces a gap in the Alfvén continuum. For a TAE with toroidal mode number n and dominant poloidal harmonics $m, m-1$, the TAE peak occurs at radial position $r = r_0$ satisfying:

$$k_{\|n,m}(r_0) = -k_{\|n,m-1}(r_0)\,. \tag{1}$$

Here the parallel wavevector $k_{\|n,m}$ is defined as:

$$k_{\|n,m}(r) = -\frac{1}{R}\left(n + \frac{m}{q(r)}\right), \tag{2}$$

where R is the major radial coordinate and $q(r)$ is the tokamak safety factor profile. The solution to equations (1) and (2) implies that TAEs occur at rational values of the safety factor profile, given by:

$$q(r_0) = -\frac{\left(m - \frac{1}{2}\right)}{n}. \tag{3}$$

The frequency ω_{gap} at the centre of the Alfvén gap is given by the product of the parallel wavevector with the plasma Alfvén speed v_{A}. The second equality in equation (4) is obtained by substituting in equations (2) and (3).

$$\omega_{\text{gap}} = k_{\|n,m}(r_0)\, v_{\text{A}}(r_0) = \frac{v_{\text{A}}(r_0)}{2Rq(r_0)}. \tag{4}$$

The TAE itself has frequency ω_{TAE} lying within the Alfvén gap. To zeroth order approximation, $\omega_{TAE} \approx \omega_{\text{gap}}$.

2.2. Heuristic description of the new model

In the linear theory, TAE-FI resonance occurs on discrete surfaces in 3D (μ, E, P_ϕ) COM space, i.e. lines in 2D (E, P_ϕ) COM space. These discrete lines are labelled by toroidal and poloidal integer mode numbers. In fact, the resonance is a nonlinear phenomenon. Here the 'linear picture' describes the resonant interaction of an unperturbed particle trajectory with a TAE; whereas the 'nonlinear picture' takes into account that the particle trajectory is itself altered by the TAE, which influences the resonant interaction. In the nonlinear theory, the Hamiltonian action-angle formalism is used to solve the COM space equations of motion, demonstrating that a resonant particle will oscillate back and forth around its original COM space position, referred to as the nonlinear bounce motion. In particular, it can be shown that particles are constrained to move along straight lines in $(\bar{P_\phi}, \bar{P_\theta})$ COM space, and oscillate around the linear resonance; the equation of motion can then be solved simply in 1D. The outer edges of this oscillation define a resonance band (or resonance region) of finite non-zero width. This resonance region may be equivalently defined as the region of COM space where particles can resonate with the mode.

The resonance line positions in 2D COM space are given by a formula from linear drift-kinetic theory (section 2.4.1). The resonance width formula (section 2.4.2) is derived from the particle Hamiltonian equations of motion. A heuristic description of this formula is that the resonance width (particle COM space oscillation width) is proportional to the line-average of the TAE potential along the unperturbed particle trajectory. Analytical approximations are used to describe the TAE structure (section 2.4.3) and the passing particle trajectories (section 2.4.5), to enable evaluation of the resonance width formula. Resonance lines and widths are calculated numerically from these formulae and plotted in 2D COM space, for qualitative visual interpretation of resonance overlap.

The primary inputs required for the ROM are the magnetic field equilibrium $\mathbf{B}(\psi,\theta)$, the TAE toroidal and poloidal mode numbers n, m, and the TAE frequency ω_{TAE}. These inputs may be obtained from experimental data, or from an analytically constructed example. From these inputs, the resonance lines (section 2.4.1) can be calculated. In order to calculate the resonance widths (section 2.4.2), the following additional inputs are required: the TAE Fourier eigenfunctions $\Phi_{nm}(\psi)$ (section 2.4.3); the particle frequencies ω_ϕ and ω_θ for each point in COM space (section 2.4.4); and the particle trajectory in the form $\left(\psi(\bar{\theta}), \theta(\bar{\theta}), \phi(\bar{\theta})\right)$ for each point in COM space (section 2.4.5). These quantities may be calculated either by running another modelling code (a linear MHD code for the TAE, and an orbit-following code for the particle trajectories), or directly from the primary inputs by means of simple analytical approximations. Here (ψ,θ,ϕ) are standard orthogonal flux coordinates parametrising real space, and $\bar{\theta}$ is an angular variable parametrising motion along the particle trajectory (defined in section 2.4.2).

The physics basis of the ROM relies on the GC approximation and the conservation of particle magnetic moment μ. These assumptions are valid only if the magnetic field does not vary substantially over the particle Larmor orbit. FIs in spherical tokamaks (STs) combine large Larmor radii with wide variations of the magnetic fields, and under these conditions the adiabatic invariance of μ can break down [33–36]. The validity of the GC assumption is not tested in this paper, since the ROM is only benchmarked against GC codes. Additionally, the formula $\mu \approx \frac{Mv_\perp^2}{2B}$ (M the particle mass) is used here for many calculations such as phase space coordinate transforms; but this is only a zeroth-order approximation to the actual adiabatic invariant μ [28, 33]. This approximation roughly corresponds to a distortion of the 2D COM space slice shown in the resonance maps. Further assumptions, required only for certain analytical approximations, are specified in sections 2.4.3–2.4.5.

This paper uses sign convention COCOS7 for equilibria with current and magnetic field in the same direction (analytical case), and COCOS3 for equilibria with current and magnetic field in opposite directions (MAST-U case), to define the sign of $q(r)$ [37]. Without loss of generality, $\mathrm{sign}(\omega_{\mathrm{TAE}})$ is taken to be positive. Since the TAE mode numbers satisfy equation (3), then they must be defined such that $\mathrm{sign}(nmq) = -1$. It remains to choose $\mathrm{sign}(n)$. In fact, the model has a strong symmetry between the cases for positive and negative n, with resonances occurring for both signs. However in tokamak experiments, typically only one sign of n is observed. This is because the driving FI gradient only drives the TAE whose sign matches the co-current direction [19]: this condition is used to select $\mathrm{sign}(n)$ in this paper.

All plots in this paper show the 2D slice $\mu = 0$ of 3D particle COM space (except some $\mu \neq 0$ cases included in appendix A.1). All plots show only the COM space region of co-current passing particles. For all plots incorporating HALO code runs, the HALO code is run in GC mode.

2.3. *Description of different model versions*

In section 3, we present five different versions of the ROM, referred to as ROM (i)–(v). Details of the five versions are given in table 1. All ROM versions use the Hamiltonian formalism detailed in section 2.4.2. The differences are in the calculation of the additional inputs by either high-performance modelling codes or analytical approximations. ROM (i) involves the most numerical inputs and is therefore the most accurate; ROM (v) is entirely analytical and therefore the fastest to compute. Results from all five versions are presented and compared in section 3.2, in order to assess the validity of the various approximations used.

Note that ROM versions (i)–(ii) apply to the whole of particle COM space. However for the purposes of this paper, the restriction to the passing particle region (where our analytical particle trajectory approximation applies) was applied identically across all model versions.

2.4. *Model equations*

All symbol and parameter definitions are listed in appendix A.2, table 4.

Table 1. Description of ROM versions.

ROM version	TAE eigenfunctions	Particle trajectories	Particle frequencies
(i)	MISHKA (full)	HALO	HALO
(ii)	MISHKA (2 modes only)	HALO	HALO
(iii)	MISHKA (2 modes only)	analytical approx.	HALO
(iv)	analytical approx.	analytical approx.	HALO
(v)	analytical approx.	analytical approx.	analytical approx.

2.4.1. Resonance lines: analytical formula.

In linear kinetic theory, the condition for resonance between a tokamak particle and a TAE (under the GC formalism) is given by [29, 38]:

$$n\omega_\phi\left(\mu,E,P_\phi\right)+l\omega_\theta\left(\mu,E,P_\phi\right)=\omega_{\mathrm{TAE}}. \tag{5}$$

Here l is any integer, which labels the different resonances (a single TAE typically has multiple resonances). ω_ϕ and ω_θ are the toroidal and poloidal angular frequencies of the GC motion: i.e. $\omega_\phi=\frac{2\pi}{\tau_\phi}$, where τ_ϕ is the average time period for the GC to traverse from $\phi=0$ to $\phi=2\pi$; and ω_θ defined similarly. Note $\omega_\theta=\frac{\partial\bar{\theta}}{\partial t}$ and $\omega_\phi=\frac{\partial\bar{\phi}}{\partial t}$. The particle frequencies ω_ϕ and ω_θ depend on the particle COM (μ,E,P_ϕ), and they can therefore be viewed as functions in COM space.

2.4.2. Hamiltonian formalism for resonance widths.

The key element of the ROM is the formula for the nonlinear width of the resonance region, derived from the particle Hamiltonian equations of motion in action-angle coordinates [22]. This is used to define a resonance region in 2D COM space, which can be plotted to qualitatively determine where different resonance regions overlap.

The key parameter describing the resonance widths is $V_{nl}(\mu,E,P_\phi)$, given by equation (6),

$$\begin{aligned}V_{nl}\left(\mu,E,P_\phi\right)=Q\sum_m\frac{1}{2\pi}\int_0^{2\pi}&\Phi_{nm}\left(\psi\right)\\&\times\left\{-i\left[\omega_{TAE}+v_\parallel\mathbf{b}\cdot\left(n\nabla\phi+m\nabla\theta\right)\right]\right\}\\&\times\exp\left[i\left(l\bar{\theta}-m\theta+n\bar{\phi}-n\phi\right)\right]\mathrm{d}\bar{\theta}.\end{aligned} \tag{6}$$

Here Q is the particle charge; $\Phi_{nm}(\psi)$ are the TAE Fourier eigenfunctions; $\mathbf{b}$ is the magnetic field unit vector; and $v_\parallel$ is the particle velocity component parallel to the magnetic field; and $(\bar{\theta},\bar{\phi})$ are the angle variables in the Hamiltonian action-angle formalism. These angle variables are defined specifically for each equilibrium (unperturbed) particle trajectory, in such a way that each particle moves with $\frac{\partial\bar{\phi}}{\partial t}=\omega_\phi$ and $\frac{\partial\bar{\theta}}{\partial t}=\omega_\theta$ constant.

The integration variable $\bar{\theta}$ parametrises the unperturbed particle trajectory; thus the V_{nl} formula describes a line-integral along the unperturbed particle trajectory, with the integrand incorporating features of the magnetic equilibrium and the TAE perturbation. All quantities in the integrand are functions of the particle spatial position $\left(\psi(\bar{\theta}),\theta(\bar{\theta}),\phi(\bar{\theta})\right)$. The particle trajectory itself is uniquely defined by the particle COM (μ,E,P_ϕ), thus V_{nl} is a function on COM space.

The sum is taken over all poloidal harmonics m of the TAE. The largest $|V_{nl}|$, and hence the strongest power transfer, occur when l is equal to one of the dominant poloidal m numbers of the TAE [22].

The nonlinear resonance width is then defined by:

$$\frac{1}{n}\delta\bar{P}_\phi=\frac{1}{l}\delta\bar{P}_\theta=2\sqrt{2}\frac{\sqrt{|V_{nl}|}}{\sqrt{\left|\left(l\frac{\partial}{\partial\bar{P}_\theta}+n\frac{\partial}{\partial\bar{P}_\phi}\right)\left(n\omega_\phi+l\omega_\theta\right)\right|}}. \tag{7}$$

An alternative definition of the resonance width is given by:

$$\begin{aligned}\delta\omega&=\delta\left(n\omega_\phi+l\omega_\theta\right)\\&=2\sqrt{2}\sqrt{\left|\left(l\frac{\partial}{\partial\bar{P}_\theta}+n\frac{\partial}{\partial\bar{P}_\phi}\right)\left(n\omega_\phi+l\omega_\theta\right)\right|}\sqrt{|V_{nl}|}.\end{aligned} \tag{8}$$

Here $(\bar{P}_\phi,\bar{P}_\theta)$ are the action variables (canonical momenta) in the Hamiltonian action-angle formalism [22]. Equation (7) describes the particle excursion in 2D $(\bar{P}_\phi,\bar{P}_\theta)$ COM space, while equation (8) describes the variation in the frequency function $(n\omega_\phi+l\omega_\theta)$ over the same excursion.

Particles are constrained to travel along straight lines of constant $n\bar{P}_\theta-l\bar{P}_\phi$ in $(\bar{P}_\phi,\bar{P}_\theta)$ space [22]. To implement the ROM, the width $\delta\omega$ is calculated for each point on the resonance line, and particles are assumed to travel along straight lines $n\bar{P}_\theta-l\bar{P}_\phi=constant$, up to the outer points where $(n\omega_\phi+l\omega_\theta)$ has varied by $\pm\delta\omega$. The set of all such outer points define the outer edges of the resonance region. Notice that since V_{nl} scales with the TAE amplitude, the resonance width $\delta\omega$ scales with the square root of the TAE amplitude.

Under the toroidal axisymmetry assumption $\bar{P}_\phi=P_\phi$, whereas $\bar{P}_\theta\neq P_\theta$. Since the calculation of $\bar{P}_\theta$ is not implemented in HALO, we use the approximation $\bar{P}_\theta=-\frac{1}{2}\frac{Q}{B_0}\bar{r}^2$ (here B_0 is the magnetic field strength at the magnetic axis) [22]. Examples of the relationship between $\bar{\theta}$ and θ are shown in figures 1(*b*) and (*d*).

2.4.3. TAE structure: analytical approximation.

One of the inputs required for the ROM is the TAE Fourier eigenfunctions $\Phi_{nm}(\psi)$ (or $\Phi_{nm}(r)$, under the circular flux surface assumption). These are typically calculated using a linear MHD code such as MISHKA. The alternative analytical approximation used in this paper is adapted from [39]. This approximation includes only the two dominant TAE poloidal harmonics. It is theoretically valid under the following assumptions:

(a) low-beta plasma, $\beta = \frac{8\pi p}{B^2} \ll 1$ (p is the plasma pressure; B is the magnetic field strength) [39–41],
(b) equilibrium with circular flux surfaces [39],
(c) high poloidal mode number, $m \gg 1$ [39, 40],
(d) weak toroidal coupling, $\tilde{\epsilon} = 2(\epsilon + \Delta'_{Shaf}) \approx \frac{5}{2}\frac{r}{R_0} \ll 1$ (r is the minor radial variable; R_0 is the tokamak major radius; $\epsilon = \frac{r}{R_0}$ is the local inverse aspect ratio parameter; $\tilde{\epsilon} = 2(\epsilon + \Delta'_{Shaf})$ is the local toroidal coupling parameter; Δ_{Shaf} is the Shafranov shift) [40, 41],
(e) low shear, $s = \frac{rq'}{q} \ll 1$ [39] .

Values of these parameters for the example TAEs used in this study are listed in table 2. Note that the analytical TAE described here is the only mode existing in the Alfvén gap provided $\epsilon \ll s^2$; otherwise, additional modes may exist in the same gap with a different analytical description [42].

The outline of the analytical TAE derivation is as follows (details in [39, 40]). First, the TAE electrostatic potential f_{TAE} is Fourier transformed, to express it in terms of Fourier components $\Phi_{nm}(r)$:

$$f_{\rm TAE}(r,\theta,\phi,t) = \sum_m \Phi_{nm}(r)\exp\left[-i\left(\omega_{\rm TAE}t + m\theta + n\phi\right)\right]. \tag{9}$$

Next, the linearised Ideal MHD equations in toroidal geometry are Fourier transformed and reduced to a set of coupled 1D ordinary differential equations in $\Phi_{nm}(r)$ [41, 43]. In cylindrical geometry, the equations for each (n,m) would be uncoupled. However, toroidal effects introduce coupling between adjacent poloidal harmonics. These effects are only significant in a narrow 'inner region' local to $r = r_0$, where adjacent continuum modes match in frequency (see equation (1)). In the 'outer region' far from $r = r_0$, toroidal coupling effects are negligible and the cylindrical solution applies. The solution for the TAE eigenfunctions $\Phi_{nm}(r)$ is derived separately under these two different limits and an asymptotic matching condition is applied. These two solutions will be referred to as $\Phi^{\rm inner}_{nm}(r), \Phi^{\rm outer}_{nm}(r)$ respectively: their exact formulae are given by equations (12),(16),(17) in [39].

For the purposes of calculating the V_{nl} integral in equation (6), it is necessary to use one continuous function $\Phi_{nm}(r)$. In this paper, we approximate the radially varying inner solution as a constant value (specifically, its maximum value $\Phi^{\rm inner,0} = \max\left\{\Phi^{\rm inner}_{n,m}(r)\right\}$). We then 'stitch together' the inner and outer solutions by applying this constant inner value as an upper cutoff or 'flat top' on the outer solution. Figures 3(c) and (d) show the accurate mode structures calculated by MISHKA, while figures 3(e) and (f) show the analytical solution with the 'flat top' approximation applied. The applicability of this approximation depends on how the orbit excursion width compares to the width scale of the inner mode structure. Throughout most of particle COM space, the particle trajectory only interacts with the inner mode structure over a very small r range, where the mode variation has a negligible effect on the integral overall.

The TAE amplitude is given in terms of $\frac{\delta B}{B}$, defined as the total magnetic field perturbation due to the TAE relative to the equilibrium magnetic field (evaluated at $r = r_0$).

2.4.4. *Particle frequencies: analytical approximation.*

The ROM also requires the particle frequencies ω_ϕ and ω_θ as inputs. These frequencies may be calculated using an orbit-following code such as HALO. Alternatively, under the assumptions of circular flux surfaces and strongly passing particles satisfying $\epsilon \ll \frac{\Delta_*}{\bar{r}} \ll 1$, the following analytical approximations may be derived [22]:

$$\omega_\phi = -\frac{v_{\parallel *}}{R_0} \tag{10}$$

$$\omega_\theta = -\frac{v_{\parallel *}}{R_0}\frac{1}{q\left(\bar{r}\right)} \tag{11}$$

where $\bar{r}$ is the particle orbit-averaged minor radial position; Δ_* is the particle orbit excursion from radial position $\bar{r}$; and $v_{\parallel *}$ is the particle parallel velocity where it crosses the $Z = Z_0$ plane on the outboard side.

2.4.5. *Particle trajectories: analytical approximation.*

The ROM also requires the particle trajectories as inputs. For the purposes of calculating the V_{nl} integral in equation (6), a particle trajectory in the form $\left(r(\bar{\theta}), \theta(\bar{\theta}), \phi(\bar{\theta})\right)$ is required for each point (μ, E, P_ϕ) in COM space. In fact, under the large aspect ratio assumption then $\bar{\phi} \approx \phi$ and the ϕ term approximately cancels out from the integrand, so only the functions $r(\bar{\theta})$ and $\theta(\bar{\theta})$ are required. Particle trajectories may be calculated either using an orbit-following code such as HALO, or a suitable analytical approximation. In this paper, two different approximations are used, for the cases of circular flux surfaces and MAST-U flux surfaces respectively.

For the case of a circular flux surface equilibrium (such as the analytical case study described in section 3.1), we use the standard formulae for strongly passing particle trajectories [22]. To construct this simple analytical model, the functions $r(\bar{\theta})$, $\theta(\bar{\theta})$ are expressed in terms of two COM space parameters $\bar{r}, \Delta_*$. Under the assumption $\epsilon \ll \frac{\Delta_*}{\bar{r}} \ll 1$, a strongly passing particle trajectory can be described by equations (12) and (13), which describe approximately circular orbits in the poloidal plane, shifted horizontally outwards off the flux surfaces by Δ_*. (For co-current passing particles, Δ_* is positive).

$$r = \bar{r} + \Delta_* \cos\theta \tag{12}$$

$$\theta = \bar{\theta} - \frac{\Delta_*}{\bar{r}}\sin\theta. \tag{13}$$

First, it is necessary to estimate the trajectory parameters $\bar{r}, \Delta_*$ for each point (μ, E, P_ϕ) in COM space. This is done using the conservation of P_ϕ. The particle must have equal values of P_ϕ everywhere on its trajectory, in particular at the two points where it crosses $Z = Z_0$ in the poloidal plane (the inboard and outboard extrema of the trajectory). The formula $P_\phi = Q\psi - MRv_\parallel$ can be used to estimate these two points. Equations (12) and (13) imply that these points are at $r = \pm\bar{r} +$

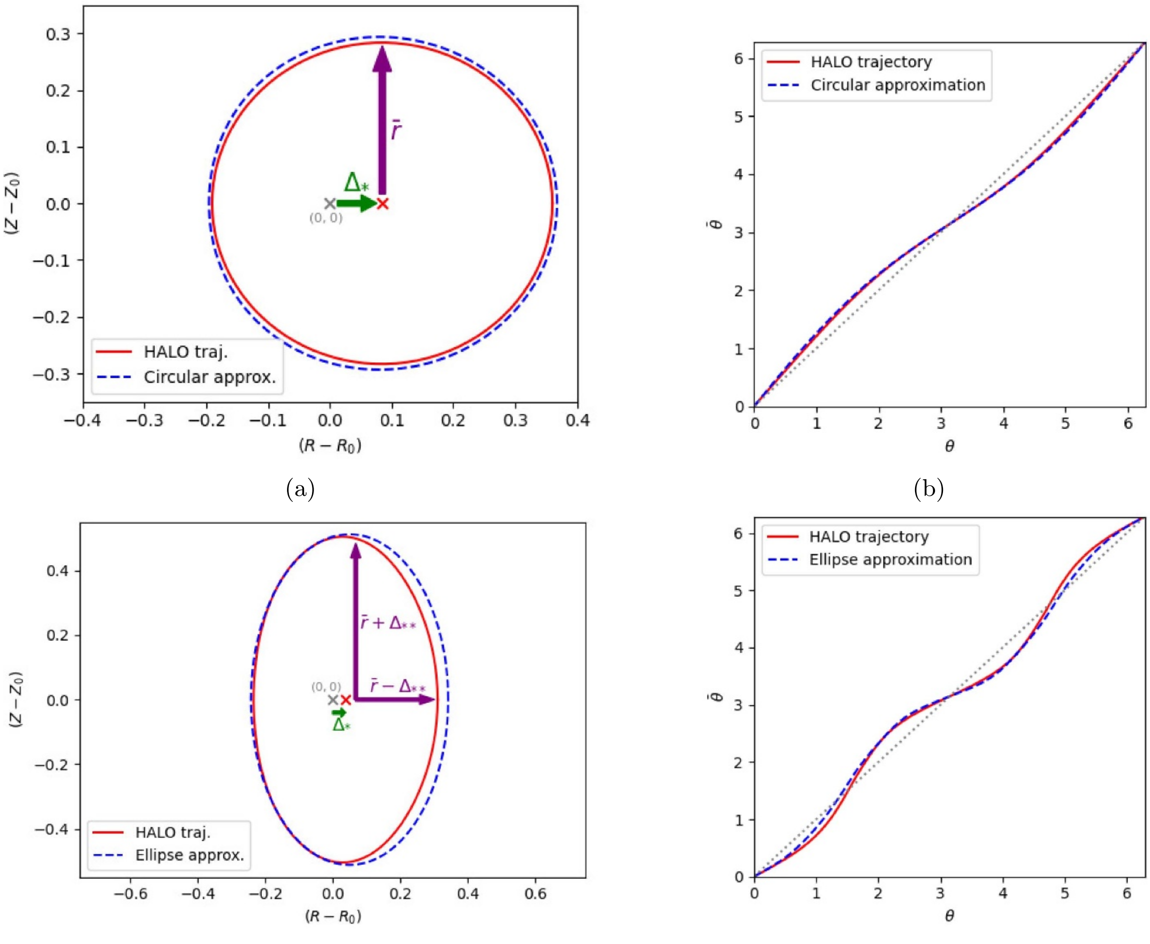

(a) (b)

(c) (d)

Figure 1. Example particle trajectory approximations. (*a*) shows the poloidal projection of the trajectory approximation used for the analytical (circular flux surface) case, for a sample particle at $E = 0.6$ MeV. The approximation is compared with the full trajectory as calculated by HALO. (*b*) shows the corresponding $\bar{\theta}(\theta)$ approximation for the analytical case, compared to a straight line (grey dotted). (*c*) shows the poloidal projection of the elliptical trajectory approximation developed for the MAST-U case, for a sample particle at $E = 60$ keV. (*d*) shows the corresponding $\bar{\theta}(\theta)$ approximation for the MAST-U case, compared to a straight line (grey dotted).

Δ_*, and this can be directly solved for $\bar{r}, \Delta_*$. Once $\bar{r}, \Delta_*$ have been obtained, equation (13) can be used to iteratively estimate $\theta(\bar{\theta})$, and then $r(\bar{\theta})$ can be calculated from equation (12). An example particle trajectory calculated by HALO, alongside the corresponding particle trajectory approximation, is shown in figure 1(*a*).

For the case of a MAST-U equilibrium (such as the case study described in section 3.1), we use an adapted trajectory model. In MAST-U, the assumption of circular flux surfaces is strongly violated. Therefore a higher-order extension to the particle trajectory formula is needed: this is motivated by observation of MAST-U particle trajectories calculated by HALO (see figures 1(*c*) and (*d*)). In particular, the poloidal orbit projection appears elliptical rather than circular, and the function $\theta(\bar{\theta})$ appears to have a substantial double-periodicity component. Accordingly, we introduce an additional parameter Δ_{**} to account for these two deviations from the circular case. We express the functions $r(\bar{\theta})$, $\theta(\bar{\theta})$ in terms of three COM space parameters $\bar{r}, \Delta_*, \Delta_{**}$. Equations (14)–(18) replace equation (12), while equation (19) replaces equation (13). Equations (14)–(18) describe an ellipse in the poloidal plane, shifted horizontally outwards off the flux surfaces by Δ_* (here $r'(\theta')$ describes an ellipse centred at $(R, Z) = (\Delta_*, 0)$, then $r(\theta)$ represents the same curve with origin $(0, 0)$). The parameter $\Delta_{**} = \frac{\Delta Z - \Delta R}{2}$ describes the ellipticity, where $\Delta Z, \Delta R$ are the major and minor radii respectively. A heuristic investigation found that the parameter $\frac{\Delta_{**}}{\bar{r}}$ provides a good approximation for the double-periodicity term coefficient required in equation (19),

$$r' = \frac{(\bar{r} - \Delta_{**})(\bar{r} + \Delta_{**})}{\sqrt{[(\bar{r} - \Delta_{**})\sin\theta']^2 + [(\bar{r} + \Delta_{**})\cos\theta']^2}} \tag{14}$$

$$R = r'\cos\theta' + \Delta_* \tag{15}$$

$$Z = r'\sin\theta' \tag{16}$$

$$r = \sqrt{R^2 + Z^2} \tag{17}$$

$$\theta = \arctan\left(\frac{Z}{R}\right) \tag{18}$$

$$\theta = \bar{\theta} - \frac{\Delta_*}{\bar{r}}\sin\theta + \frac{\Delta_{**}}{\bar{r}}\sin 2\theta \tag{19}$$

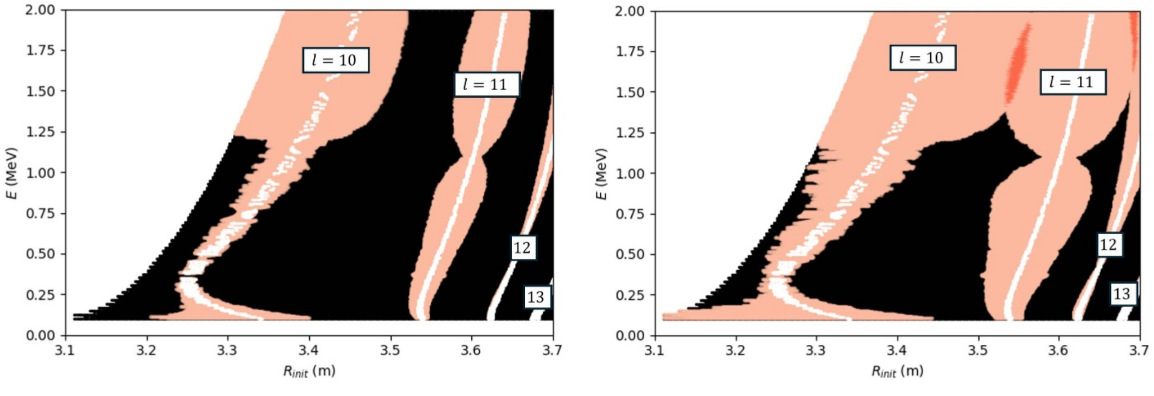

(a)

(b)

Figure 2. Example resonance maps produced by the ROM, for the analytical case study with the $n = -6$ TAE. (*a*): mode amplitude $\frac{\delta B}{B} = 0.004$. (*b*): mode amplitude $\frac{\delta B}{B} = 0.016$. Maps produced by ROM (iii). In figure 2(*b*) the amplitude is quadrupled relative to figure 2(*a*), so the resonance widths are approximately doubled.

Again, we estimate the trajectory parameters $\bar{r}, \Delta_*, \Delta_{**}$ from (μ, E, P_ϕ) using the conservation of P_ϕ. A similar method is used, except that the calculation involves the vertical extrema of the particle trajectory as well as the horizontal extrema. Once $\bar{r}, \Delta_*, \Delta_{**}$ have been obtained, the functions $r(\bar{\theta})$ and $\theta(\bar{\theta})$ can be calculated from equations (14)–(19). An example particle trajectory calculated by HALO, alongside the corresponding particle trajectory approximation, is shown in Figure 1*(c)*.

Figure 1 shows only one randomly chosen particle trajectory for each case, to illustrate the approximations. More comprehensive benchmarking is carried out in section 3.2, by comparing the resonance maps produced when the particle trajectories are calculated either by HALO or by this approximation, for two case study equilibria. The model can be generalised to different equilibria by finding a suitable representation of the particle trajectories.

2.5. *Example resonance map*

Results of the ROM are produced in the form of ‘resonance maps’ for qualitative interpretation. Figure 2 shows example resonance maps produced for the analytical equilibrium case study with the $n = -6$ TAE (section 3.1), for two different values of mode amplitude ($\frac{\delta B}{B} = 0.004, 0.016$). This figure illustrates the square root scaling of resonance width with mode amplitude: in figure 2(*b*) the amplitude is quadrupled relative to figure 2(*a*), so the resonance widths are approximately doubled.

The resonance map depicts 2D particle COM space in coordinates (R_{init}, E), for a fixed value of the third COM space coordinate μ (in this paper always $\mu = 0$). The background black region depicts the region of COM space where co-current passing particle orbits can exist. White lines indicate the resonance lines associated with the specified TAE(s). Pale pink regions indicate the nonlinear resonance regions associated with each TAE resonance line, as calculated by the Hamiltonian formalism. Darker pink regions show the overlap of two or more resonance regions.

Irregular features in the plotting of resonance lines and the boundaries of resonance regions, such as those seen towards the left of figure 2(*b*), are a result of numerical error. Small numerical errors in the resonance width are magnified at the stage of the calculation where the COM space parametrisation is converted from (E, P_ϕ) to $(E, \bar{r})$. This effect is worse at lower $\bar{r}$ values (i.e. lower R_{init} values), especially for the analytical case study: this is because $\frac{\partial P_\phi}{\partial r} \sim \frac{\partial \psi}{\partial r}$ is very small for low r values.

3. Example results from the new model

In this section, example results of the ROM are displayed and analysed. We apply the ROM to two example cases, an analytically constructed equilibrium and a MAST-U equilibrium.

3.1. *Case studies*

The first case study is taken from HALO code benchmarks [19]. It consists of an analytically constructed equilibrium, along with an $n = -6$ TAE. The equilibrium has circular flux surfaces as shown in figure 3(*a*), large aspect ratio, and low shear. The TAE is strongly dominated by two main poloidal harmonics, as shown in figure 3(*c*). Notice that the analytical TAE described in section 2.4.3 is a very suitable approximation for this case, since the parameters $s(r_0), \tilde{\epsilon}(r_0)$ are indeed $\ll 1$ (details listed in table 2). For all resonance maps produced for this case study, the maximum particle energy is set at 2 MeV. This is an arbitrary high energy value chosen mainly to contrast with the MAST-U case study (see below), particularly regarding the dimensionless orbit shift parameter $\frac{\Delta_*}{\bar{r}}$ (whose importance is discussed in section 3.3). The analytical equilibrium at 2 MeV has $\frac{\Delta_*}{\bar{r}}$ in the range $\sim 0.4 - 0.8$, whereas the MAST-U equilibrium at 100 keV has $\frac{\Delta_*}{\bar{r}} \sim 0.1 - 0.3$.

The second case study equilibrium is reconstructed from MAST-U discharge #47133, at 225 ms. This discharge was chosen because two well-separated TAEs are clearly identifiable, and some FI transport is observed. Summary

Table 2. Parameters describing the TAEs studied in the analytical and MAST-U cases.

Parameter	Analytical case: $n = -6$ TAE	MAST-U case: $n = 2$ TAE	MAST-U case: $n = 3$ TAE
Dominant poloidal mode numbers $m-1, m$	11,12	3,4	4,5
Safety factor crossover $q(r_0) = -\frac{\left(m-\frac{1}{2}\right)}{n}$	1.92	−1.75	−1.5
TAE central location r_0 [m]	0.331	0.260	0.174
Major radius R_0 [m]	3.068	0.939	0.939
TAE frequency f_{TAE} (calculated by MISHKA) [kHz]	76.1	56.2	66.4
Alfvén gap frequency $f_{gap} \approx \frac{1}{2\pi}\frac{v_{\mathrm{A}}(r_0)}{2R_0 q(r_0)}$ [kHz]	71.4	45.5	61.1
Local shear $s(r_0)$	0.150	0.650	0.213
Local toroidal coupling parameter $\tilde{\epsilon}(r_0)$	0.269	0.693	0.463
Assumed constant plasma density value n_e $[cm^{-3}]$	5.0×10^{13}	2.0×10^{13}	2.0×10^{13}

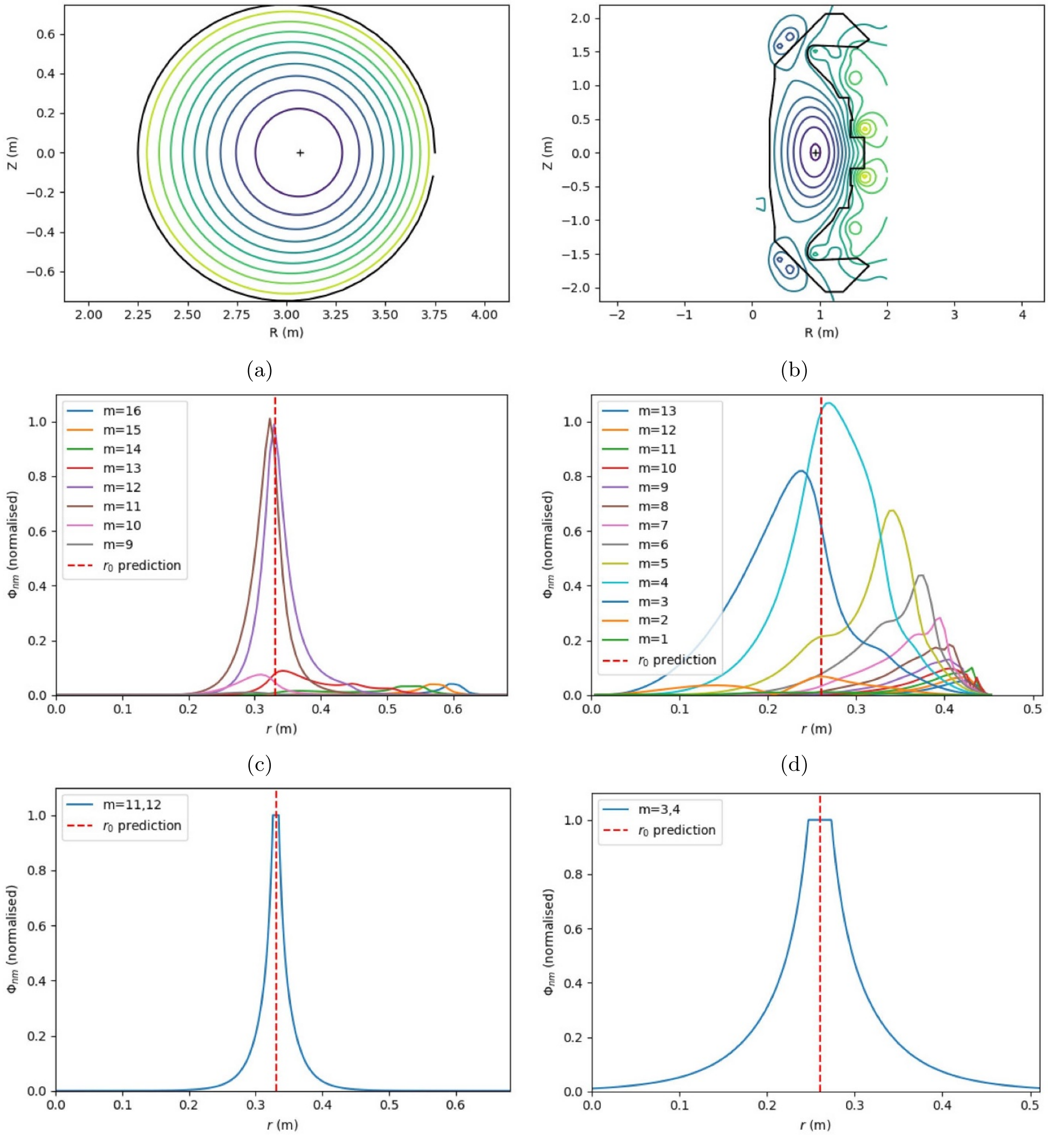

(a) (b)

(c) (d)

(e) (f)

Figure 3. Magnetic equilibria and TAE radial profiles for the two case studies. (*a*) and (*b*) show the flux surfaces in the poloidal plane for the analytical and MAST-U cases respectively. (*c*) and (*d*)) show the MISHKA TAE profiles for the analytical $n = -6$ and MAST-U $n = 2$ cases respectively. (*e*) and (*f*) show the corresponding analytical TAE approximations for the analytical and MAST-U cases respectively.

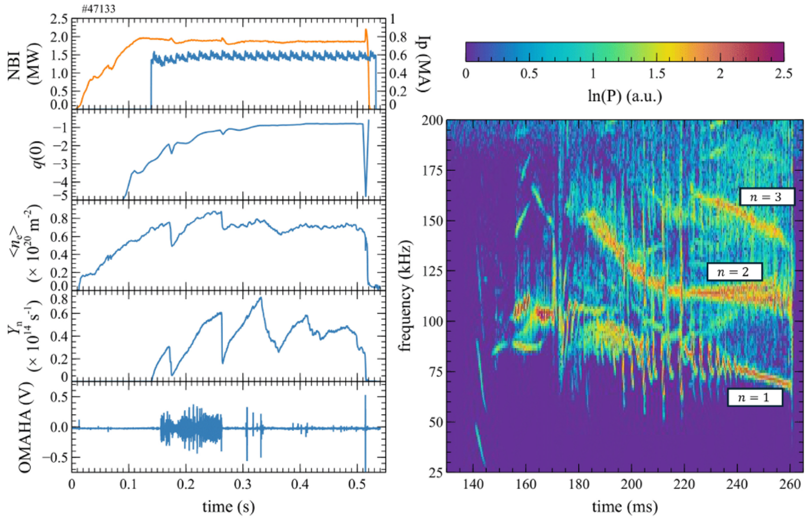

Figure 4. MAST-U diagnostic data from discharge #47133. Left panel: NBI power; plasma current; safety factor at the magnetic axis; line-integrated electron density; fission chamber neutron count; OMAHA coil CH01 signal. Right panel: MHD mode spectrogram, calculated as Fourier Transform of OMAHA coil CH01. TAEs are observed in the frequency range of 100 – 170 kHz.

Table 3. Direct comparison of $\frac{\delta B}{B}$ overlap threshold predictions by the five ROM versions, for four different cases.

ROM version	Analytical case: main two resonances ($l = 10, 11$)	Analytical case: next two resonances ($l = 11, 12$)	MAST-U case: main two resonances ($l = 3, 4$)	MAST-U case: next two resonances ($l = 4, 5$)
(i)	0.012	0.012	0.049	0.063
(ii)	0.016	0.013	0.113	0.064
(iii)	0.014	0.014	0.074	0.042
(iv)	0.017	0.016	0.091	0.023
(v)	NA ($l = 10$ out of range)	0.018	0.046	0.018

parameters from this discharge are shown in figure 4, and the equilibrium flux surfaces are shown in figure 3(*b*). Magnetic perturbations including TAEs are diagnosed on MAST-U using a magnetic pick-up coil array called OMAHA [2, 44]. The OMAHA spectrogram in figure 4 shows three clear modes in the time period of around 225–260 ms. The OMAHA signal can also be used to identify the toroidal mode numbers of these perturbations as $n = 1, 2, 3$ (from lowest to highest frequency respectively). The $n = 1$ mode is assumed to be the tail-end of a fishbone rather than a TAE, therefore only the $n = 2, 3$ modes are included in this paper. In the spectrogram, these modes are observed in the frequency range of $100 - 170$ kHz: the observed frequencies are given by $f_{\text{observed}} = f + nf_{\text{rot}}$, where f_{rot} is the toroidal rotation frequency of the plasma (estimated to be ∼33 kHz in this case), and f is the actual TAE frequency (specified for 225 ms in table 2). Unless otherwise stated, resonance maps for this case study are produced for the $n = 2$ TAE only, whose radial structure is shown in figure 3(*d*). Notice that the analytical TAE described in section 2.4.3 is a very weak approximation to this case, since the parameters $s(r_0), \tilde{\epsilon}(r_0)$ are not substantially smaller than 1 (details listed in table 2), and the two main poloidal harmonics are strongly coupled with many side harmonics. For all resonance maps produced for this case, the maximum particle energy is set at 100 keV (since MAST-U fast deuterons typically have energies up to ∼75 keV).

For both case studies, a constant plasma density profile is used. The chosen density value is specified in table 2.

3.2. Model results and discussion

Results from the ROM are produced for the five different simplification levels discussed in section 2.3. Figure 5 shows the full resonance maps, while table 3 shows the estimated resonance overlap thresholds.

The key result from figure 5 is that the resonance map remains reasonably similar across all five ROM versions (with some exceptions detailed below). This implies that resonance overlap can be reasonably well quantified even when all HALO and MISHKA outputs are replaced by simple analytical approximations. Figure 5 also allows us to identify which approximations introduce the greatest degree of inaccuracy, so future improvements to the model can focus on updating these with more advanced or higher order approximations as required.

Table 3 quantifies the degree of error. For the analytical case, all ROM versions agree to within ∼50% of each other. For the MAST-U case, all ROM versions agree to within a

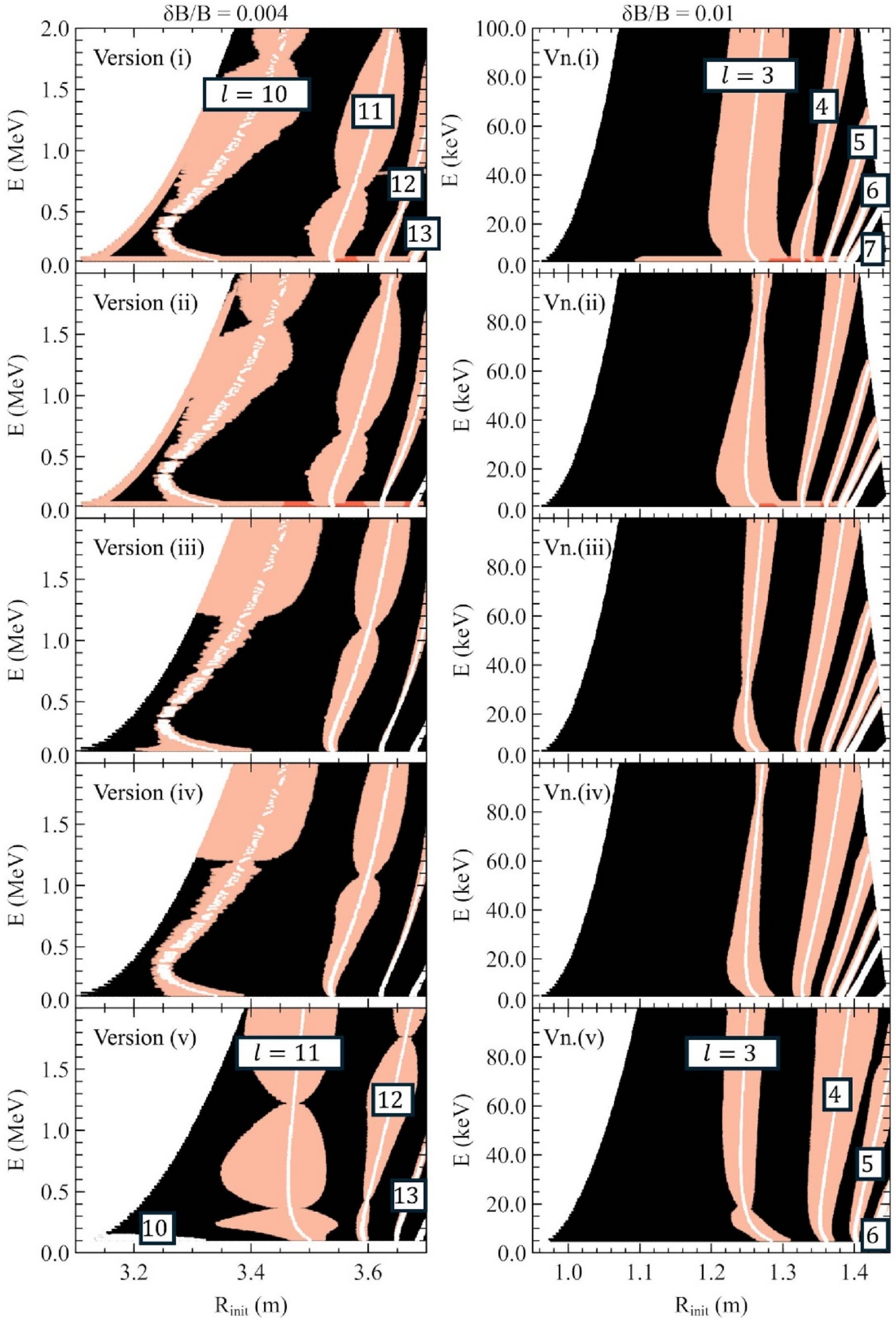

Figure 5. Direct comparison of resonance maps produced by the five ROM versions. Plots in the left column are for the analytical case study with the $n = -6$ TAE, with $\frac{\delta B}{B} = 0.004$. Plots in the right column are for the MAST-U case study with the $n = 2$ TAE, with $\frac{\delta B}{B} = 0.01$.

factor of 2.5 for the two main resonances, and a factor of 4 for the next two resonances.

For the analytical case, none of the individual approximations alter the estimated thresholds by more than $\sim 20\% - 30\%$, with the exception of the particle frequency approximations (equations (10) and (11)), which introduce the greatest inaccuracy. This is clear from the left column of figure 5: applying the particle frequency approximations (ROM (iv) to (v)) substantially alters the positions of the resonance lines, since these are very sensitive to changes in the particle frequency functions. One reason for this inaccuracy is that the particle energies (up to 2 MeV) are sufficiently high that one of the assumptions used to derive the particle frequencies ($\frac{\Delta_*}{\bar{r}} \ll 1$) breaks down. This can be demonstrated using the approximate analytical formula for Δ_* [22]:

$$\Delta_* \approx \frac{M}{QB_0} q(\bar{r}) \frac{\left(v_{\parallel *}^2 + \frac{1}{2} v_{\perp *}^2\right)}{v_{\parallel *}}$$
$$= \frac{M}{QB_0} q(\bar{r}) v_{\parallel *} = \frac{\sqrt{2M}}{QB_0} q(\bar{r}) \sqrt{E} \approx 0.00007 \cdot q(\bar{r}) \sqrt{E\,[eV]}. \tag{20}$$

For the core region $\bar{r} \lesssim 0.3$, the safety factor is $q(\bar{r}) \approx 1.9$. This gives $\Delta_* \approx 0.00014 \cdot \sqrt{E}$ and $\frac{\Delta_*}{\bar{r}} \gtrsim 0.0005 \cdot \sqrt{E}$. Thus at

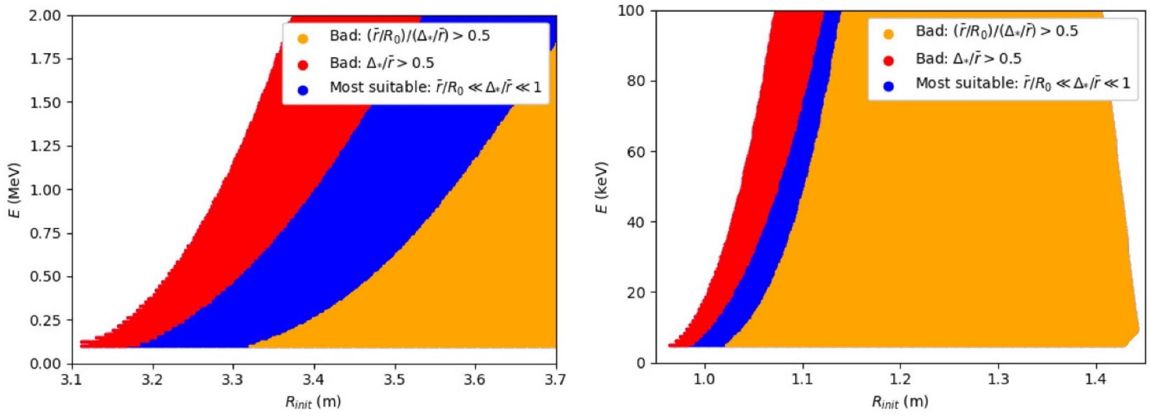

(a) (b)

Figure 6. Plots to show the approximate validity region of the assumption $\epsilon \ll \frac{\Delta_*}{\bar{r}} \ll 1$, required for the particle frequency formulae. Blue region where both inequalities hold; orange region where left inequality is approx violated; red region where right inequality is approx violated. (*a*): for the analytical equilibrium. (*b*): for the MAST-U equilibrium.

$E = 1$ MeV we have $\frac{\Delta_*}{\bar{r}} \gtrsim 0.5$ in the core region, and $\frac{\Delta_*}{\bar{r}} \gtrsim 1$ for $\bar{r} \lesssim 0.15$. The higher the energy and/or the closer to the core, the more the assumption $\frac{\Delta_*}{\bar{r}} \ll 1$ is violated. The exact validity region is shown in figure 6(*a*) (the red region shows where $\frac{\Delta_*}{\bar{r}} > 0.5$). However, it is useful to note that although the positions of the resonance lines change from ROM (iv)–(v), the resonance widths and overall overlap thresholds do not change substantially.

For the MAST-U case, by far the greatest inaccuracy is introduced by ROM (i)–(ii), i.e. reducing the many-harmonic MISHKA TAE down to only its two dominant harmonics: this increases the estimated overlap threshold by a factor of 2.3. This is somewhat unsurprising since the high-shear equilibrium in MAST-U ($s \approx 0.65$ at the peak TAE location) results in many non-negligible side harmonics of the TAE, as shown in figure 3(*d*). When applying the ROM to high-shear scenarios, a substantial improvement could be provided by using a more appropriate high-shear TAE approximation, able to capture the multiple harmonics. There is a lack of analytical global TAE theory in this area; developments would be desirable. Another improvement could be provided by using higher-order particle frequency approximations, especially in the plasma edge region ($R_{\text{init}} \gtrsim 1.35$). Figure 5 shows that the positions of the edge resonances change substantially from ROM (iv)–(v). The model currently uses the simplest, lowest-order versions of these particle frequency formulae, which fail to take into account MAST-U plasma edge effects such as the large increase in shear and the strong Shafranov shift; figure 6(*b*) also shows that the large aspect ratio assumption is violated over most of phase space (orange region). Using a more appropriate higher-order adaptation to the particle frequency formulae would be a straightforward way to upgrade ROM (v) for MAST-U. Another substantial inaccuracy of $\sim$45% is introduced by using the analytical TAE profile (i.e. ROM (iii)–(iv)) in the plasma edge region. The analytical TAE profile is scaled to have the correct peak amplitude, so it matches the MISHKA profile reasonably well in the core region; whereas its global shape and width are defined by the parameters $\tilde{\epsilon}(r_0), s(r_0)$, which strongly violate the modelling assumptions of $\tilde{\epsilon} \ll 1$, $s \ll 1$. This means the analytical TAE profile is a very poor approximation to the MISHKA profile in the edge region (see figures 3(*d*) and (*f*)). Again, a more appropriate high-shear, low-aspect-ratio TAE approximation would be very useful to improve the model results. The remaining approximations each alter the estimated overlap thresholds by around $\sim 20\% - 30\%$, without substantially altering the overall appearance of the resonance maps.

For both the analytical and MAST-U cases, a large portion of the remaining discrepancies can be explained by the highly sensitive V_{nl} 'waist' effects, discussed in section 3.3.

3.3. Discussion of V_{nl} parameter and 'waist' effects

Instead of simply using V_{nl} to calculate the nonlinear resonance widths along each resonance line, it is also enlightening to plot V_{nl} over the entire COM space slice, as shown in figure 7. This is useful in explaining some of the discrepancies between different ROM versions. The left column of figure 7 is for the analytical case with $n = -6, l = 11$; this corresponds to the second resonance line from the left in the left column of figure 5. The right column of figure 7 is for the MAST-U case with $n = 2, l = 3$; this corresponds to the leftmost resonance line in the right column of figure 5. The appropriate resonance line is overlaid onto figure 7 as a white line. The nonlinear width at each point on this resonance line is calculated from the value of V_{nl} at that point, via equation (7).

Due to the analytical behaviour of the integral in equation (6), V_{nl} is predicted to be an oscillatory function over COM space. Specifically, a simple approximation shows that each term m of the summation is proportional to $J_{m-l}\left(\frac{m\Delta_*}{\bar{r}}\right)$, where J_i is the ith Bessel function of the first kind [22, 45]. These oscillations can be clearly seen in figure 7 in the analytical case, which shows alternating bands of much higher and lower V_{nl} values. Where the resonance line crosses these bands, 'bulges' and 'waists' are seen in the corresponding resonance region. Figure 7 shows that the V_{nl} calculation overall

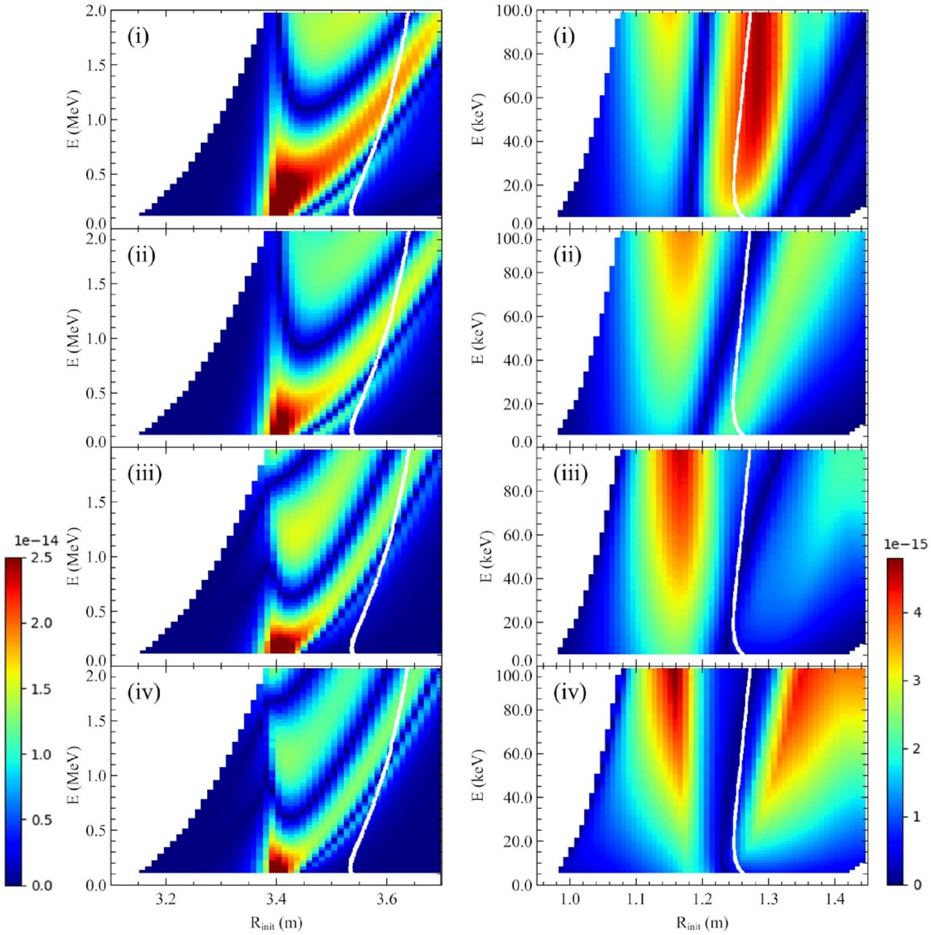

Figure 7. Direct comparison of V_{nl} parameter as a function over COM space, calculated by the ROM versions (i)–(iv). Plots in the left column (with left colourbar) are for the analytical case with $n = -6, l = 11$; plots in the right column (with right colourbar) are for the MAST-U case with $n = 2, l = 3$. The corresponding resonance line, where the V_{nl} value must be sampled to produce resonance maps, is overlaid as a white line. V_{nl} is here normalised to $\frac{\delta B}{B} = 1$.

gives heuristically similar results across ROM (i)–(iv) for the analytical case; however, slight variations cause the resonance line to sample the bulges and waists in very different positions. This reflects what is seen in figure 5: the maximum widths of each resonance region remain fairly similar across all model versions, but the waist positions move substantially. Therefore the more reduced ROM versions give good predictions of the overall picture, but very poor predictions at specific energy values, due to this ‘waist’ sensitivity.

A similar effect is seen in the MAST-U case, although here the heuristic similarity is less strong. Across ROM versions (i)–(iv), figure 7 shows two ‘lobes’ of high V_{nl} either side of a ‘waist’ of very low V_{nl}. The dramatic difference between ROM (i)–(ii) in the right column of figure 5 is partially explained by this: the position of the low band moves slightly, in such a way that the $l = 3$ resonance line samples the highest V_{nl} for ROM (i), but the lowest V_{nl} for ROM (ii). Figure 7 shows that the dramatic difference between ROM versions (i)–(ii) is mainly caused to this V_{nl} ‘waist’ sensitivity, and therefore the two-mode assumption may not be as bad as it initially seemed.

One consequence of this discussion is as follows. The overall agreement between different ROM versions looks heuristically much better for V_{nl} plots like figure 7 than for resonance maps like figure 5. However, both cases shown in figure 5 have a sparse number of resonance lines (4-5), since only one TAE is shown in each. In cases where there are many TAEs and/or each TAE has many resonance lines close together in COM space, the bulge and waist effects would become a small detail on the overall picture, and the different ROM versions may actually show better heuristic agreement.

3.4. Computational efficiency

The ROM provides significant computational reductions compared to existing methods. One reduction is that each particle trajectory need only be calculated over one poloidal rotation, with time period $\tau_\theta = \frac{2\pi}{\omega_\theta}$. (This is equivalent to calculating the equation (6) integral from $\bar{\theta} = 0$ to 2π.) In contrast, orbit-following and/or QL methods must track the particle trajectory for at least the nonlinear bounce time τ_b of the resonant interaction (see sections 2.2 and 4.2 for further details), or launch a large number of particles at different phases over the nonlinear bounce. Typically $\tau_\theta \ll \tau_b$ by several orders of magnitude, thus the ROM provides a theoretical reduction in computation time. The ROM also has the advantage that it can be run without requiring any high-performance orbit-following or linear MHD codes, including in cases where very minimal diagnostic data is provided: it only requires a magnetic equilibrium file along with the TAE mode numbers and frequencies. This allows for a greatly simplified user workflow, and is useful for rapidly testing multiple scenarios when detailed diagnostic data is not immediately accessible.

Note that the ROM computation time increases linearly with the number of resonances plotted.

4. Benchmarking of the new model

In this section, we benchmark the ROM against the HALO code. HALO is an orbit-following code with the functionality to track many particle trajectories in the presence of a TAE perturbation. This allows for explicit, accurate calculation of resonance regions and resonance overlap. We use two different approaches to compare the ROM results in section 3.2 against HALO results. The first approach (section 4.1) is to produce Poincaré plots [19]. These plots show only a 1D slice of particle COM space, with the other dimension measuring the phase difference between the particle and the wave. Particles trapped in a TAE resonance appear as closed 'islands' on a Poincaré plot, from which the resonance width can be measured. The second approach (section 4.2) is to calculate the net energy transfer between each particle and the TAE. In theory, the resonance regions should correspond with regions of highest net energy transfer.

4.1. Model benchmarking against HALO Poincaré plots

Poincaré plots can be used to precisely measure the resonance width at any given point in COM space. Examples of such plots are shown in figure 8. To produce them, HALO tracks the trajectories of several test particles in the presence of a TAE perturbation. Each time the particle crosses $\theta = 0$, the wave phase $(l\theta + n\phi - \omega_{\mathrm{TAE}}t)$ at the particle's toroidal location is recorded, and a point is plotted. Here the particles are initialised for a range of R_{init} values at a fixed (E, μ). The Poincaré plot shows R_{init} on the horizontal axis and the wave phase on the vertical axis. Non-resonant particles appear as straight lines $R_{\mathrm{init}} \approx constant$, i.e. their COM space position remains unchanged, exhibiting no coherence with the TAE. Resonant particles appear as closed islands on the Poincaré plot, since their TAE wave phase undergoes harmonic oscillations. The maximum radial width of the resonant island is the resonance width. When the resonant islands begin to overlap, stochastic behaviour is suddenly observed (seen in figure 8(*b*)).

HALO Poincaré plots were used to produce resonance width estimates for particles at different energies and mode amplitudes. In figure 9, these estimates were overlaid onto resonance maps produced by ROM (i) (the most accurate ROM version). The HALO Poincaré plot results agree reasonably well with the ROM predictions, in the sense that wherever the ROM predicts a resonance region, a resonance region of very similar width is seen in the Poincaré plots.

However, many small additional resonances appear in the Poincaré plots which do not match with any of the resonance lines predicted by equation (5). An example is the very narrow resonance appearing at $R \approx 3.58$ m in figures 8(*a*) and 9(*a*). Other authors have called these nonlinear resonances [46–48]. The presence of additional resonances could reduce the overall overlap threshold, an effect which is not included in the ROM.

4.2. Model benchmarking against HALO energy transfer plots

To produce energy transfer plots, HALO tracks the trajectories of many test particles in the presence of a TAE perturbation. At each timestep, the power transfer $P(t) = Q\mathbf{E}(t) \cdot \mathbf{v}(t)$ is calculated (where $\mathbf{E}$ is the TAE electric field and $\mathbf{v}$ is the particle velocity) [4]. The total net energy transfer $\int_0^{t_{\mathrm{end}}} P(t)\mathrm{d}t$ (where t_{end} is the end time of the calculation) is saved for each particle. Energy transfer plots provide information over all of COM space, in particular over a 2D slice comparable to that used in figure 5. The main disadvantage of energy transfer plots is that they do not show resonance regions with clearly defined edges, so they can only provide very rough estimates for the resonance overlap threshold.

HALO energy transfer plots for the analytical case study are shown in figure 10. Notice that in figures 10(*b*) and (*c*), the strongest energy transfer does not occur on the linear resonance lines, but rather on a non-resonant band centred at $R \approx 3.38$ m (corresponding to the peak TAE location). This suggests that non-resonant effects dominate over resonant effects, at least in the core region. These strong non-resonant effects are essentially caused by the extremely steep TAE profile. Non-resonant particles experience regular random 'kicks' from the TAE perturbation, but these kicks average out rapidly over time. Therefore the net energy transfer accumulated by a non-resonant particle is limited by the size of one or a few TAE 'kicks'. On the other hand, a particle in resonance with the TAE accumulates 'kicks' with a given sign of power transfer. If the variation in particle COM due to TAE resonance is neglected, then the net energy transfer of a resonant particle steadily accumulates over time, so it must eventually outstrip any non-resonant particle. However, when nonlinear effects are taken into account, the resonant particle actually follows a slow nonlinear bounce oscillation around the resonance in COM space, with timescale denoted τ_b. The positive power transfer it experiences on one side of the resonance is offset by the negative power transfer it experiences on the other side. Therefore $\int_0^{t_{\mathrm{end}}} P(t)\mathrm{d}t$ never exceeds $\int_0^{\tau_b} P(t)\mathrm{d}t$, which is proportional to both the bounce timescale τ_b and the local mode amplitude $f_{\mathrm{TAE}}(r)$. Since the amplitude of this TAE varies by many orders of magnitude between the peak and the edge, and since τ_b is sufficiently short for the resonant particles in this case, then a single 'kick' for a non-resonant particle close to the peak TAE can easily exceed $\int_0^{\tau_b} P(t)\mathrm{d}t$

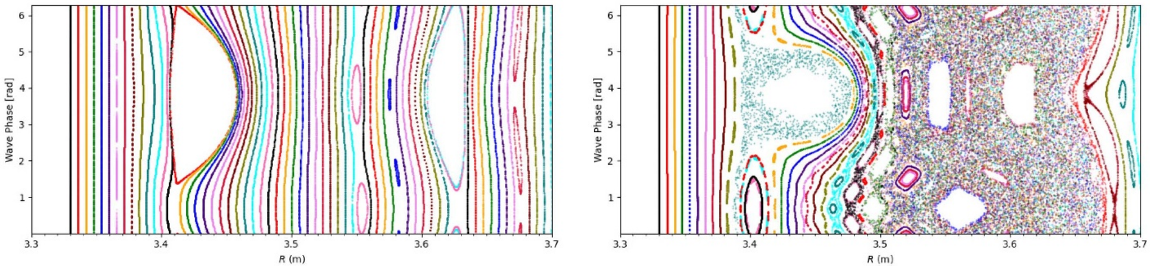

(a) (b)

Figure 8. HALO Poincaré plots for 64 particles at $\mu = 0$, $E = 1.5$ MeV, in the presence of the MISHKA $n = -6$ TAE, for the analytical case study. (*a*) is for mode amplitude $\frac{\delta B}{B} = 0.003$ (non-overlapping resonances); (*b*) is for mode amplitude $\frac{\delta B}{B} = 0.012$ (overlapping resonances causing stochasticity). Each line shows the path of one particle, with the colours chosen arbitrarily to distinguish each particle.

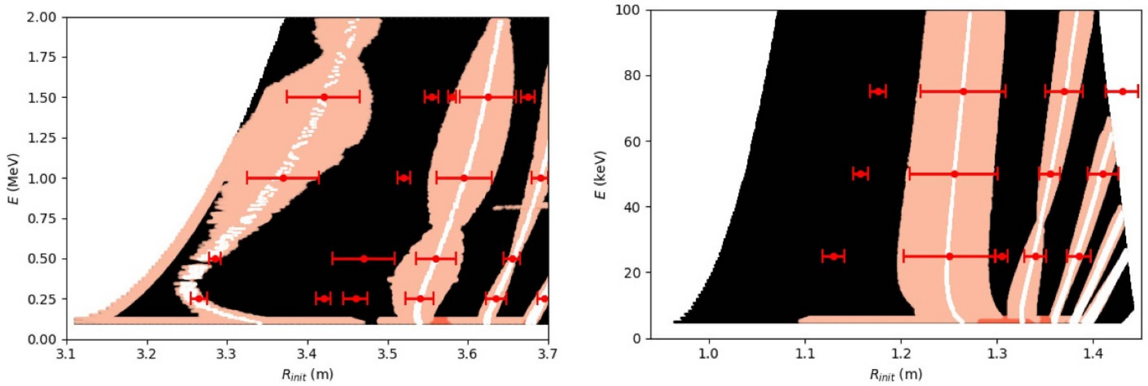

(a) (b)

Figure 9. Resonance maps produced by ROM (*i*), with resonance width data from HALO Poincaré plots overlaid as red bars. (*a*): analytical case study, $n = -6$ TAE, $\frac{\delta B}{B} = 0.003$. (*b*): MAST-U case study, $n = 2$ TAE, $\frac{\delta B}{B} = 0.01$. Note that the bars at $E = 1.5$ MeV in figure 9(*a*) are taken directly from figure 8(*a*). Resonance line l values as labelled in figure 5.

for a resonant particle far from the peak TAE. For the analytical case study, these non-resonant effects dominate over resonant effects, meaning that the HALO energy transfer plots are of limited usefulness for calculation of resonance overlap thresholds. However, the ROM (i) overlap threshold predictions ($\frac{\delta B}{B} \sim 0.01$ for first overlap at $E = 1.25$ MeV, $\frac{\delta B}{B} \sim 0.02$ for overlap in the range $1 - 1.5$ MeV) seem at least plausible, since figure 10 shows the core resonances stop being clearly separated at around $\frac{\delta B}{B} \sim 0.01 - 0.02$.

HALO energy transfer plots for the MAST-U case study are shown in figure 11. The regions of highest energy transfer are centred on the linear resonance lines, implying that non-resonant effects are insignificant in this case. Although the exact threshold of resonance overlap is unclear, it can be estimated by observing when the core resonance lines are no longer clearly separated. They show very clear separation at $\frac{\delta B}{B} = 0.001$; begin to merge at $\frac{\delta B}{B} = 0.01$; and by $\frac{\delta B}{B} = 0.04$ the individual resonance lines are no longer visible. This is in reasonable agreement with ROM (i), which predicts overlap thresholds of $\frac{\delta B}{B} \sim 0.05$ at $E = 100$ keV, $\frac{\delta B}{B} \sim 0.04$ at $E = 50$ keV, and $\frac{\delta B}{B} \sim 0.03$ at $E = 25$ keV. The edge resonances are too close together to produce any clear overlap threshold estimate.

5. Possible applications of the new model

5.1. Use cases

We make the distinction between two possible use cases of the ROM.

The first use case is the application to pre-existing data obtained from plasma discharges that have already occurred. In this case, the inputs required for the ROM can typically be obtained from diagnostic data, as is done for the MAST-U case study in this work (see section 3.1). In particular, for a given point in time, the excited TAEs can be identified from the spectrogram. Their toroidal and poloidal mode numbers can be deduced from magnetics data. If amplitude data is not available, we can make the assumption that all TAEs have equal amplitude, and estimate the overlap threshold amplitude based on this assumption. If amplitude data is available, we can input the actual individual TAE amplitudes, and accurately identify whether resonance overlap is occurring at this time (and in which regions of COM space). This use case is suitable for purposes of model validation, and to help interpret the FI behaviour that occurred during a given discharge.

Figure 12 shows an example of this for the MAST-U case study (#47133 at 225 ms), with the $n = 2, 3$ modes included

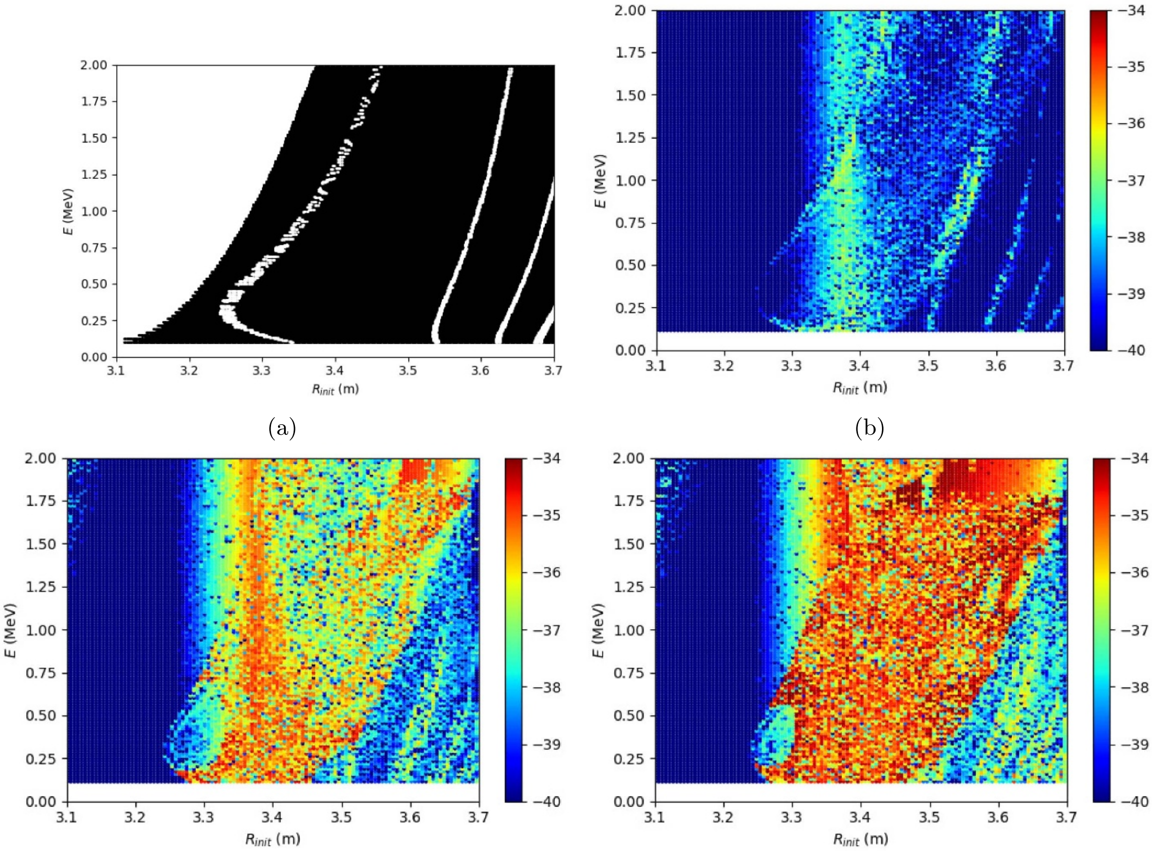

(a) (b) (c) (d)

Figure 10. HALO plots showing the logarithm of the absolute value of the net energy transfer in Joules, for 16 384 test particles over a scan of COM space, in the presence of the MISHKA $n = -6$ TAE, for the analytical case study. (*a*): positions of linear resonance lines. (*b*)–(*d*): energy transfer for mode amplitudes $\frac{\delta B}{B} = 0.001, 0.01, 0.02$ respectively. Individual resonance lines are somewhat visible when the amplitude is below the ROM overlap threshold prediction (approx. $\frac{\delta B}{B} \sim 0.01 - 0.02$), but no longer visible when the threshold is exceeded. Resonance line l values as included in figure 5.

as identified from the spectrogram. Since sufficient amplitude data was not available, we only predict an overlap threshold amplitude (assuming both TAEs have equal amplitude), and do not determine whether this threshold was exceeded. Note that when more TAEs are included, the overlap threshold becomes lower. Since this figure only shows co-current passing particles with $\mu = 0$, the overlap threshold may be substantially different for other regions of COM space.

This paper will be followed by a second study, using a similar method to validate the ROM against experimental data.

The second use case is the predictive capability for future tokamak plasma scenarios in the design stage. In this case, diagnostic data is not available. The spectrum of TAEs must be predicted by a linear MHD solver. However, this presents the question of which TAEs actually are excited (driven unstable), which depends on the FI distribution and several damping mechanisms. One option is to include the full linear spectrum of TAEs in the ROM, and identify a lower bound overlap threshold (provided this threshold is *not* exceeded, overlap will certainly *not* occur). If a more detailed answer is needed, other models must be used to first predict TAE stability, and only the excited TAEs then included in the ROM. Further complexities would arise from the possible nonlinear interactions between TAE stability and the FI distribution.

The ROM could also be used in conjunction with a critical gradient model [14, 15]. To implement a CGM, first some subset of TAEs are identified as most likely unstable, then some saturation rule is established between the FI gradient and the TAE amplitudes. Crucially the CGM is only valid under the assumption of resonance overlap (since this allows the FI distribution to diffuse and settle on the CGM prediction). Once a CGM calculation has been performed and the TAE amplitudes calculated, a subsequent ROM calculation could be used to check whether the resonance overlap assumption is indeed met.

5.2. Lower/upper bound overlap threshold estimates

It is useful to consider whether the ROM can be adapted to produce lower/upper bound resonance overlap threshold estimates. Figure 5 and table 3 show 'moderately accurate' estimates, but exhibit substantial non-monotonicity between model versions, with some overpredicting and some underpredicting. This non-monotonicity is difficult to avoid since equation (6)

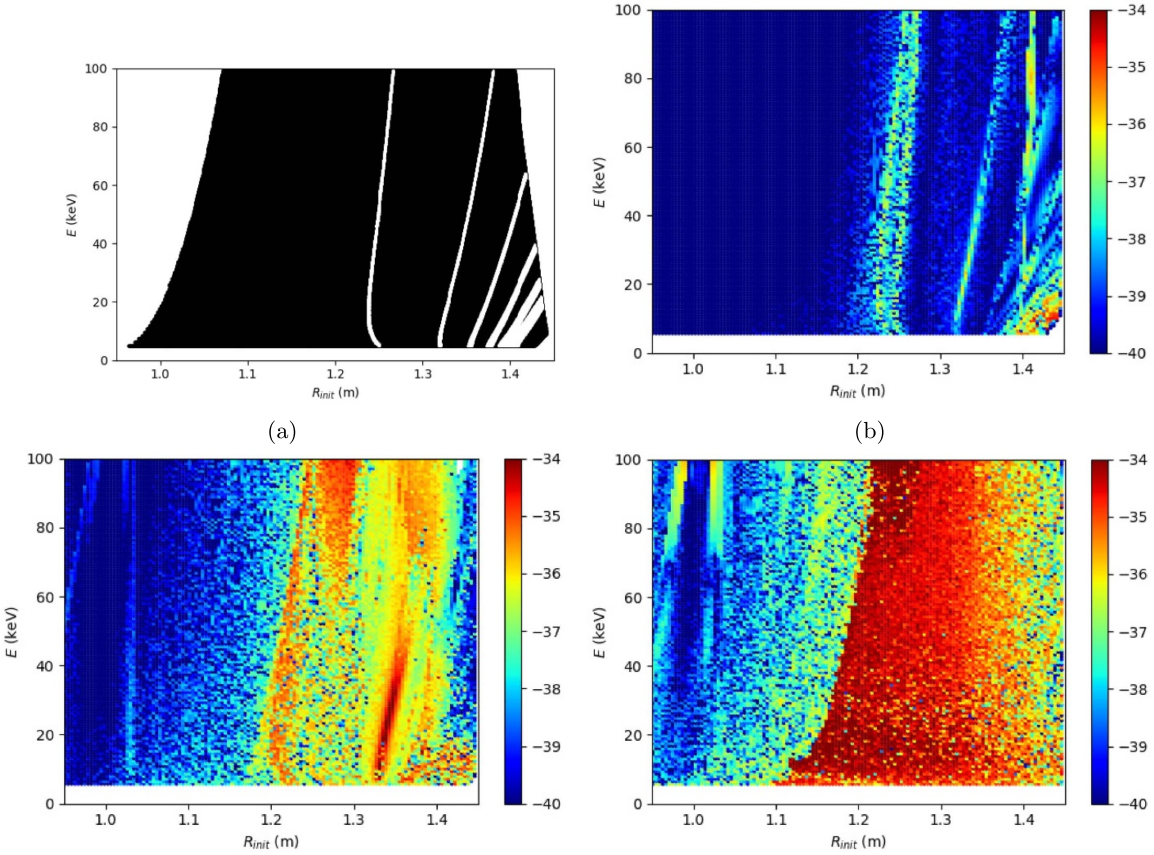

(a) (b)

(c) (d)

Figure 11. HALO plots showing the logarithm of the absolute value of the net energy transfer in Joules, for 16 384 test particles over a scan of COM space, in the presence of the MISHKA $n = 2$ TAE, for the MAST-U case study. (*a*): positions of linear resonance lines. (*b*)–(*d*): energy transfer for mode amplitudes $\frac{\delta B}{B} = 0.001, 0.01, 0.04$ respectively. Individual resonance lines are somewhat visible when the amplitude is below the ROM overlap threshold prediction (approx. $\frac{\delta B}{B} \sim 0.04 - 0.05$), but no longer visible when the threshold is reached. Resonance line l values as included in figure 5.

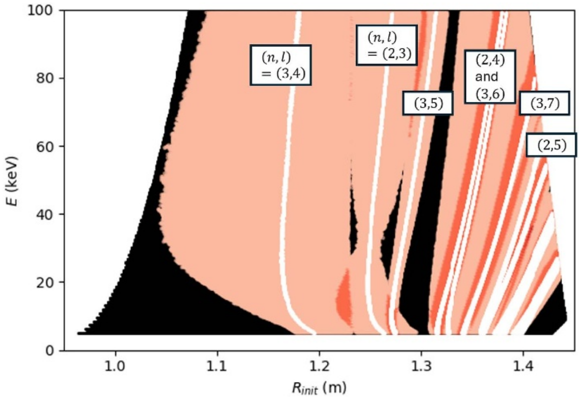

Figure 12. Resonance map produced by ROM (iii) for the MAST-U case study: realistic scenario with $n = 2, 3$ TAEs included. This plot is for $\frac{\delta B}{B} = 0.036$, the estimated overlap threshold for the core resonances.

is oscillatory in nature, and these oscillations depend sensitively on the Fourier harmonics of the different terms in the integrand.

Due to the 'waist' structure resulting from these oscillations (discussed in section 3.3), the resonance widths are reduced to near zero at certain (fairly sensitive and unpredictable) points in COM space. This makes it difficult to find a sensible lower bound for the resonance width (other than zero), therefore difficult to find an upper bound for the overlap threshold $\frac{\delta B}{B}$. Some solutions are available: we can lower bound the width of the *widest* point (or 'bulge'), using a similar method to equations (21)–(23) below; then calculate when it touches the ideal (zero width) resonance line of the neighbouring resonance. This would allow us to guarantee that 'if $\frac{\delta B}{B}$ exceeds this threshold value, *some* resonance overlap certainly does occur at *some* energies'.

On the other hand, it is relatively straightforward to calculate an upper bound for the resonance width, i.e. a lower bound for the overlap threshold. For practical applications, this allows us to guarantee that 'provided $\frac{\delta B}{B}$ stays *below* this threshold value, overlap certainly does *not* occur'. (Note that this lower bound only applies to the passing particle region as currently formulated; thresholds in the trapped particle region may be lower.) Depending on the amount of detailed information available (on the mode structure etc), the lower bound may be tuned 'tighter' or 'looser'. A very loose lower bound, which can be calculated with even very limited information, is given as follows. We produce the resonance maps using an upper bound on V_{nl}:

$$\begin{aligned} |V_{nl}|\left(\mu,E,P_{\phi}\right) \leqslant Q\sum_{m}\Bigg\{ & \max|\Phi_{nm}|\max_{\text{orbit}}|\omega_{\text{TAE}}-v_{\parallel}k_{\parallel nm}|\,\frac{1}{2\pi} \\ & \times\left|\int_{0}^{2\pi}\exp\left[i\left(l-m\right)\bar{\theta}+im\frac{\Delta_{*}}{\bar{r}}\sin\bar{\theta}\right]\mathrm{d}\bar{\theta}\right|\Bigg\}. \end{aligned} \tag{21}$$

Here we have applied the LAR approximation $\bar{\phi}\approx\phi$, and the circular flux surface orbit approximation (equation (13)), in the exponential term: we find these approximations have a sufficiently small effect that the bound still applies even in the MAST-U case. We have also rewritten $\mathbf{b}\cdot(n\nabla\phi+m\nabla\theta)=-k_{\parallel nm}$. We then apply the Jacobi-Anger expansion to evaluate the integral:

$$\begin{aligned} |V_{nl}|\left(\mu,E,P_{\phi}\right) \leqslant Q\sum_{m}\max|\Phi_{nm}|\max_{\text{orbit}}|\omega_{\text{TAE}} & \\ -v_{\parallel}k_{\parallel nm}|\left|J_{|l-m|}\left(m\frac{\Delta_{*}}{\bar{r}}\right)\right| & \qquad (22) \\ \leqslant Q\sum_{m}\max|\Phi_{nm}|\max_{\text{orbit}}|\omega_{\text{TAE}}-v_{\parallel}k_{\parallel nm}|\,P\left(l-m\right). & \qquad (23) \end{aligned}$$

Here J_{α} is the Bessel function of the first kind of order α, and we define the function $P(\alpha)=\max_{x}|J_{|\alpha|}(x)|$.

This method has the advantage that $\max|\Phi_{nm}|$ can be calculated straightforwardly from $\frac{\delta B}{B}$, even when the mode structure $\Phi_{nm}(r)$ is not known. Another major advantage is that equation (23) is much simpler to calculate than equation (6), since the integral has already been evaluated analytically. Preliminary calculations suggest that equation (23) underestimates the overlap threshold $\frac{\delta B}{B}$ by a factor of around 5 to 20 times in the core plasma region, compared to ROM (i). (Using $\max|\Phi_{nm}|$ causes it to underestimate much more drastically in the edge region away from the peak TAE.) This bound can be improved upon if more information is available, for example by replacing $\max|\Phi_{nm}|$ with $\max_{\text{orbit}}|\Phi_{nm}(r)|$, and by treating $(\omega_{\text{TAE}}-v_{\parallel}k_{\parallel nm})$ with a higher order Fourier transform.

Further analytical investigations, taking advantage of this Bessel function reduction, will be published in a future work.

6. Discussion and conclusions

In this work, we develop a new reduced ROM to calculate TAE resonance regions in particle phase space, enabling the calculation of phase-space-dependent TAE resonance overlap thresholds. This threshold determines stochasticity of FI transport by TAEs. The ROM is based on an analytical framework described in [22]: it is highly reduced compared to previous methods, since it bypasses the need for computationally intensive orbit-following and linear MHD codes. The ROM is of interest for implementation as a submodule in transport codes, and for rapid qualitative assessment of the effect of different plasma parameters on resonance overlap. In this work, we apply the ROM to the passing particle region: promising results suggest that the model is worth further investigation and development, such as an extension to the trapped particle region. We intend to cover this in a future work.

We present five different versions of the ROM. ROM (i) incorporates outputs from the HALO and MISHKA codes; each subsequent version replaces these outputs one-by-one with simple analytical approximations; up to ROM (v) which is entirely analytical. This multi-step formulation enables the accuracy of each approximation to be assessed individually. For practical application, it also provides the freedom to select a model version based on accuracy/efficiency requirements.

We test the five ROM versions on two contrasting case studies: an analytically constructed plasma equilibrium and a MAST-U equilibrium reconstructed from experimental data. The analytical equilibrium is chosen as a 'best-case scenario' since it satisfies all the modelling assumptions very well; the MAST-U equilibrium is chosen as a 'worst-case scenario' since it falls well outside the applicability range of most of the modelling assumptions. For the analytical case, overlap thresholds calculated by the different ROM versions agree to within $\sim$50% across most of phase space. For the MAST-U case, overlap thresholds calculated by the different ROM versions differ by up to a factor of 2.5 in the plasma core region, but by up to a factor of 4 in the plasma edge region. This reflects the fact that many of the modelling assumptions are strongly violated near the MAST-U plasma edge. Further optimisation of the ROM for STs such as MAST-U would be possible by adapting the analytical approximations used, particularly the analytical TAE approximation and the particle frequency approximations. However, even in its present non-optimised form, the ROM does provide moderately good estimates for resonance overlap thresholds in the MAST-U plasma core.

We benchmark the ROM against HALO code simulations, since orbit-following codes of this type provide the standard tools used in the literature to produce TAE resonance maps. Resonance widths calculated by the ROM show good agreement with resonance widths calculated from HALO Poincaré plots, for both the analytical and MAST-U cases.

The key advantage of the ROM compared to previous computational methods is that it can produce TAE resonance maps from a quick and simple calculation, requiring only a magnetic equilibrium file and the TAE mode numbers and frequencies as inputs. Existing reduced FI transport models rely on linear MHD solvers to compute the modes; whereas results from ROM (i)–(iv) suggest that resonance overlap thresholds are not particularly sensitive to the finer details of the mode structure, only to the peak mode amplitude, which substantially reduces the computational requirements. The key advantage of the ROM compared to previous theoretical formalisms is that it produces full resonance maps over most of phase space, rather than relying on reducing the problem down to 1D. It is also highly adaptable to diverse plasma scenarios, with less reliance on strong assumptions such as neglecting orbit excursion. Another advantage of the ROM is that it generalises easily to scenarios with many TAEs present.

Figure 7 suggests that the resonance regions are highly sensitive to the particle trajectory parameters and the Bessel function structure described in [45]. Figures 5 and 7 also show that some phase-space resolution (particularly energy resolution) is lost as the model is reduced from ROM (i) to (v), in a large part due to this Bessel function structure. However, ROM (v) can still provide reasonable estimates for the onset of large-scale resonance overlap throughout the plasma region.

There are several important limitations to consider, when applying the ROM to different tokamak scenarios. First, the ROM is based on the GC assumption, which is known to be problematic for FIs in STs: further benchmarking against full-orbit calculations is needed to quantify this error. Second, the TAE approximation used here relies on the assumptions of large aspect ratio and low shear, since the analytical theory of TAEs has not been developed for STs. Third, the basic particle trajectory formulae rely on the assumption of circular flux surfaces; adapted formulae are needed for equilibria with non-circular flux surfaces, since the resonance width calculation is very sensitive to this shaping. Fourth, the particle frequency formulae rely on not only the circular flux surface assumption (violated in STs), but also the assumption of $\epsilon \ll \frac{\Delta_*}{r} \ll 1$ (violated for particles with very high energy and/or large orbit excursion width, and for particles near the plasma edge in STs). Each approximation may be tested by substituting more accurate modelling code outputs instead, and comparing the results (similarly to ROM (i)–(v) in this paper). The ROM inherently contains the freedom to adapt its various analytical approximations for different plasma scenarios: for example, low-order large-aspect-ratio formulae may be substituted out for higher-order formulae more suited to STs.

The ROM may be applied to interpret diagnostic data from plasma discharges, or in a predictive capacity to assist design of future plasma scenarios. The ROM may be adjusted to produce most accurate estimates or lower/upper bound estimates, depending on the requirements and the available data. Of particular importance is detailed information on the TAE spectrum, including stability and amplitudes. If only lower bound overlap thresholds are required, it may be sufficient to include the entire linear spectrum of TAEs, whether or not they are excited: overlap certainly will not occur below this threshold. It is also straightforward to tune the model equations to produce true lower bound overlap threshold estimates, which can be even more highly reduced analytically. True upper bound estimates are generally more difficult to obtain, but can be found if we relax the COM-space-resolution of the model. (Note that if only upper bound overlap thresholds are required, then it may be sufficient to restrict the ROM to the passing particle region as formulated in this paper: overlap certainly occurs once this threshold is reached, but may occur sooner in other COM space regions).

This paper will be followed by a validation of the ROM against experimental data.

Acknowledgments

The authors are grateful to Prof. Marco Cecconello (Uppsala University Sweden) for reviewing this paper. This work has been supported by the Fusion Centre for Doctoral Training. This work was supported by the EPSRC Energy Programme [Grant Number EP/W006839/1]. This work was supported by the U.S. Department of Energy Contract DEFG02-04ER54742.

Appendix

A.1. Resonance maps for $\mu \neq 0$

Hitherto in this paper, all figures have shown the $\mu = 0$ slice of COM space. Figure 13 shows the effect of varying μ, for the analytical case study. The same amplitude value $\frac{\delta B}{B} = 0.015$ is used in all plots.

These figures only show the passing particle COM space region. As μ increases, we have excluded more and more of COM space, since it contains either trapped orbits (approx bottom region of plot), or stagnation or potato orbits (approx left region of plot). Note that the trapped particle region is given by $E < \mu B(R_{\text{init}})$.

The key point to observe from this figure is that the overlap threshold (in the passing particle region) remains reasonably similar across all μ values, for the analytical case study. The same situation was found for the MAST-U case study. This informs the choice to show only $\mu = 0$ plots in the body of this paper. However, different case studies may exhibit stronger dependence on μ. In general, when using the ROM to estimate resonance overlap thresholds, it is advisable to produce resonance maps at a few different μ values, as in figure 13.

For the case $\mu B_0 = 1$ MeV (figure (13(c))), we produced HALO Poincaré plots and plotted the resonance width data as red bars. The resonance widths and overlap threshold agree reasonably well: for example at $E = 1.8$ MeV, the overlap threshold is almost reached but not quite. However, the red bars appear systematically shifted ~ 0.05 m to the left as compared to the ROM plot. There may be some systematic difference in the approximations used to initiate the particles and calculate μ; this discrepancy may require some further investigation.

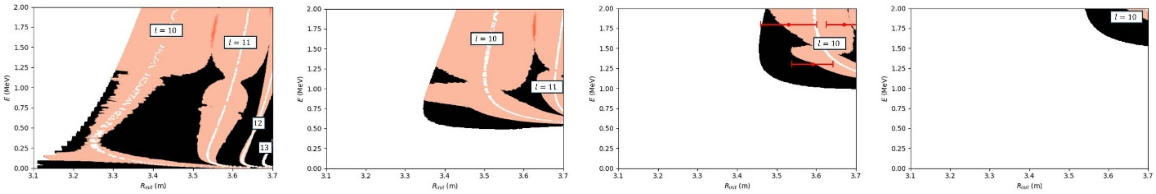

(a) (b) (c) (d)

Figure 13. Resonance maps produced by ROM (iii) for the analytical case study with the $n = -6$ TAE, at varying values of μ, all with $\frac{\delta B}{B} = 0.015$. (*a*): $\mu B_0 = 0.0$ MeV. (*b*): $\mu B_0 = 0.5$ MeV. (*c*): $\mu B_0 = 1.0$ MeV. *d*): $\mu B_0 = 1.5$ MeV. In (*c*), resonance width data from HALO Poincaré plots is overlaid as red bars.

A.2. List of symbols, parameters and acronyms

See tables 4 and 5.

Table 4. Symbol and parameter definitions.

Constants	
Q	Particle charge
M	Particle mass
R_0	Magnetic axis radial coordinate (major radius)
Z_0	Magnetic axis vertical coordinate
Variables parametrising real space	
r	Minor radial variable
ψ	Poloidal flux function (alternative radial variable to r; under circular flux surface assumption then $\psi = \psi(r)$)
(R, Z)	Horizontal/vertical Cartesian variables parametrising poloidal plane (i.e. major radial coordinate and vertical coordinate)
(ϕ, θ)	Toroidal and poloidal angle variables in orthogonal flux coordinates (ψ, θ, ϕ)
$(\bar{\phi}, \bar{\theta})$	Toroidal and poloidal angle variables in action-angle formalism. Defined differently for each particle trajectory; they are defined such that the particle moves with $\frac{\partial \bar{\phi}}{\partial t}, \frac{\partial \bar{\theta}}{\partial t}$ constant.
Variables parametrising COM space	
E	Particle constant of motion: energy
μ	Particle constant of motion: magnetic moment
P_ϕ	Particle constant of motion: toroidal canonical angular momentum
$(\bar{P_\phi}, \bar{P_\theta})$	Particle constants of motion: toroidal and poloidal action variables (momenta) in action-angle formalism. (Note that under toroidal axisymmetry assumption, $\bar{P_\phi} = P_\phi$.)
$\bar{r}$	Average minor radius of particle trajectory (alternative parameter to P_ϕ)
R_{init}	Particle major radial position, when it crosses the magnetic axis on the outboard side (alternative parameter to $\bar{r}$)
$v_{\parallel *}$	Particle velocity parallel to the magnetic field, when it crosses the magnetic axis on the outboard side (alternative parameter to E)
σ	Extra parameter for sign of direction of particle motion
Other features of particle trajectories	
$\omega_\phi, \omega_\theta$	Angular frequencies of particle periodic motion in toroidal, poloidal directions respectively. (I.e. $\omega_\phi = \frac{2\pi}{\tau_\phi}$, where τ_ϕ is the average time period for the particle to traverse from $\phi = 0$ to $\phi = 2\pi$; and ω_θ defined similarly.) Functions on COM space (μ, E, P_ϕ). Note $\omega_\theta = \frac{\partial \bar{\theta}}{\partial t}$ and $\omega_\phi = \frac{\partial \bar{\phi}}{\partial t}$.
Δ_*	Particle orbit excursion width (radial shift from flux surfaces). Function on COM space (μ, E, P_ϕ).
$\Delta R, \Delta Z, \Delta_{**}$	Additional parameters introduced to describe MAST-U elliptical orbits. Functions on COM space (μ, E, P_ϕ).
$v_\parallel$	Particle velocity parallel to magnetic field. Varies along particle trajectory.

(Continued.)

Table 4. (Continued.)

Features of the magnetic equilibrium	
B	Magnetic field vector
b	Magnetic field unit vector
v_A	Alfvén speed profile
q	Safety factor profile
s	Shear profile $s = \frac{rq'(r)}{q(r)}$
Δ_{Shaf}	Shafranov shift parameter
ϵ	Local inverse aspect ratio parameter, $\epsilon = \frac{r}{R_0}$
$\tilde{\epsilon}$	Local toroidal coupling parameter, $\tilde{\epsilon} = \frac{r}{R_0} + \Delta'_{Shaf} \approx \frac{5}{2}\frac{r}{R_0}$
Parameters to describe TAEs	
r_0	Minor radial position of TAE peak. Defined by $q(r_0) = -\frac{(m-\frac{1}{2})}{n}$, for a TAE with dominant poloidal harmonics $m, m-1$.
ω_{TAE}	TAE frequency
n, m	TAE toroidal, poloidal mode numbers
l	An integer labelling different resonances with the same TAE. Strongest power transfer occurs when l is equal to one of the poloidal m mode numbers of the TAE.
$\frac{\delta B}{B}$	TAE amplitude—given in terms of magnitude of magnetic field perturbation relative to equilibrium magnetic field (evaluated at r_0).
$k_{\parallel nm}$	Spatially varying Shear Alfvén parallel wavevector in toroidal geometry: $k_{\parallel nm} = -\frac{1}{R}\left(n + \frac{m}{q}\right)$
$f_{TAE}(\psi, \theta, \phi, t)$	TAE electrostatic potential
$\Phi_{nm}(\psi)$	TAE Fourier amplitude functions
Resonance width parameters	
V_{nl}	Function on particle COM space, describing the TAE perturbation amplitude averaged over the whole particle trajectory (for a particular TAE with toroidal mode number n; and a particular resonance line labelled by l)
$\delta\bar{P_\phi}, \delta\bar{P_\theta}$	Width of particle wobble from its original $(\bar{P_\phi}, \bar{P_\theta})$ COM space position, caused by resonance with TAE
$\delta\omega$	Variation of particle frequency function $(n\omega_\phi + l\omega_\theta)$ from its original value, caused by resonance with TAE

Table 5. Acronyms used in this paper.

Acronym	Meaning
COCOS	COordinate COnventionS
COM	Constants of motion
FI	Fast ion
GC/FO	Guiding-centre / full-orbit
HALO	An orbit-following code: combination of the HAGIS+LOCUST codes
LAR	Large aspect ratio
MAST-U	MAST-Upgrade: a spherical tokamak device
MHD	Magnetohydrodynamic
MISHKA	A linear MHD code: used to calculate TAE profiles
NBI	Neutral beam injection
ROM	Reduced Resonance Overlap Model: the new model presented in this paper
ST	Spherical tokamak
TAE	Toroidal Alfvén eigenmode

ORCID iDs

R. Blyth 0009-0003-8736-0489
B.N. Breizman 0000-0002-7908-6497

References

[1] Fasoli A. *et al* 2007 Chapter 5: physics of energetic ions *Nucl. Fusion* **47** S264

[2] Rivero-Rodríguez J.F. *et al* 2024 Overview of fast particle experiments in the first MAST Upgrade experimental campaigns *Nucl. Fusion* **64** 086025

[3] Heidbrink W.W. 2008 Basic physics of Alfvén instabilities driven by energetic particles in toroidally confined plasmasa *Phys. Plasmas.* **15** 055501

[4] Sharapov S.E. 2012 Toroidal Alfvén eigenmodes and fast particles in tokamaks *Fusion Sci. Technol.* **61** 104–12

[5] Fredrickson E.D., Gorelenkov N.N., Bell R.E., Menard J.E., Roquemore A.L., Kubota S., Crocker N.A. and Peebles W. 2006 Fast ion loss in a ‘sea-of-TAE *Nucl. Fusion* **46** S926

[6] Berk H.L., Breizman B.N. and Ye H. 1993 Map model for nonlinear alpha particle interaction with toroidal Alfvén waves *Phys. Fluids B* **5** 1506–15

[7] Wang H. *et al* 2025 Nonlinear excitation of energetic particle driven geodesic acoustic mode by resonance overlap with Alfvén instability in ASDEX Upgrade *Sci. Rep.* **15** 1130

[8] Chirikov B.V. 1979 A universal instability of many-dimensional oscillator systems *Phys. Rep.* **52** 263–379

[9] Collins C.S., Heidbrink W.W., Podestà M., White R.B., Kramer G.J., Pace D.C., Petty C.C., Stagner L., Van Zeeland M.A. and Zhu Y.B. 2017 Phase-space dependent critical gradient behavior of fast-ion transport due to Alfvén eigenmodes *Nucl. Fusion* **57** 086005

[10] Mikhailovskii A.B., Huysmans G.T.A., Kerner W.O.K., Sharapov S.E. 1997 Optimization of computational MHD normal-mode analysis for tokamaks *Plasma Phys. Rep.* **23** 844–57

[11] Cheng C.Z. 1992 Kinetic extensions of magnetohydrodynamics for axisymmetric toroidal plasmas *Phys. Rep.* **211** 1–51

[12] Berk H.L., Breizman B.N., Fitzpatrick J. and Wong H.V. 1995 Line broadened quasi-linear burst model [fusion plasma] *Nucl. Fusion* **35** 1661

[13] Gorelenkov N.N., Duarte V.N., Podesta M. and Berk H.L. 2018 Resonance broadened quasi-linear (RBQ) model for fast ion distribution relaxation due to Alfvénic eigenmodes *Nucl. Fusion* **58** 082016

[14] Ghantous K., Gorelenkov N.N., Berk H.L., Heidbrink W.W. and Van Zeeland M.A. 2012 1.5D quasilinear model and its application on beams interacting with Alfvén eigenmodes in DIII-D *Phys. Plasmas.* **19** 092511

[15] Bass E.M. and Waltz R.E. 2019 Prediction of Alfvén eigenmode energetic particle transport in ITER scenarios with a critical gradient model *Nucl. Fusion* **60** 016032

[16] Podestà M., Gorelenkova M. and White R.B. 2014 A reduced fast ion transport model for the tokamak transport code TRANSP *Plasma Phys. Control. Fusion.* **56** 055003

[17] Lauber P., Falessi M., Meng G., Hayward-Schneider T., Popa V.-A., Zonca F. and Schneider M. 2024 ATEP: an advanced transport model for energetic particles *Nucl. Fusion* **64** 096010

[18] Gorelenkov N.N., Pinches S.D. and Toi K. 2014 Energetic particle physics in fusion research in preparation for burning plasma experiments *Nucl. Fusion* **54** 125001

[19] Fitzgerald M., Buchanan J., Akers R.J., Breizman B.N. and Sharapov S.E. 2020 HALO: a full-orbit model of nonlinear interaction of fast particles with eigenmodes *Comput. Phys. Commun.* **252** 106773

[20] Oliver H.J.C. *et al* 2023 Toroidal Alfvén eigenmodes observed in low power JET deuterium-tritium plasmas *Nucl. Fusion* **63** 112008

[21] Todo Y., Van Zeeland M.A. and Heidbrink W.W. 2016 Fast ion profile stiffness due to the resonance overlap of multiple Alfvén eigenmodes *Nucl. Fusion* **56** 112008

[22] Breizman B. and Sharapov S. 2025 *Confinement and Stability of Fast Ions in Fusion Plasmas by Boris Breizman, Sergei Sharapov - Waterstones.* (Taylor & Francis Ltd.) (www.waterstones.com/book/confinement-and-stability-of-fast-ions-in-fusion-plasmas/boris-breizman/sergei-sharapov/9781032185330)

[23] Berk H.L. and Breizman B.N. 1990 Saturation of a single mode driven by an energetic injected beam. I. Plasma wave problem *Phys. Fluids B* **2** 2226–34

[24] Berk H.L. and Breizman B.N. 1990 Saturation of a single mode driven by an energetic injected beam. II electrostatic ‘universal’ destabilization mechanism *Phys. Fluids B* **2** 2235–45

[25] Berk H.L. and Breizman B.N. 1990 Saturation of a single mode driven by an energetic injected beam. III. Alfvén wave problem *Phys. Fluids B* **2** 2246–52

[26] Berk H.L., Breizman B.N. and Pekker M. 1996 Nonlinear Dynamics of a Driven Mode near Marginal Stability *Phys Rev Lett.* **76** 1256–9

[27] Breizman B. 2010 Nonlinear consequences of energetic particle instabilities *Fusion Sci. Technol.* **59** 549–60

[28] Littlejohn R.G. 1983 Variational principles of guiding centre motion *J. Plasma Phys.* **29** 111–25

[29] Porcelli F., Stankiewicz R., Kerner W. and Berk H.L. 1994 Solution of the drift-kinetic equation for global plasma modes and finite particle orbit widths *Phys. Plasmas.* **1** 470–80

[30] Goldstein H. 1980 Chapter 10 Hamilton-Jacobi Theory *Classical Mechanics* 2nd edn (Addison-Wesley) p 457

[31] Gorelenkov N.N. and White R.B. 2012 Perturbative study of energetic particle redistribution by Alfvén eigenmodes in ITER *Plasma Phys. Control. Fusion.* **55** 015007

[32] Kolesnichenko Y.I., Patten H., Lutsenko V.V., Graves J.P. and Rudenko T.S. (JET Contributors) 2021 Ion cyclotron resonance heating with shifted separatrix *Nucl. Fusion* **61** 046014

[33] Belova E.V., Gorelenkov N.N. and Cheng C.Z. 2003 Self-consistent equilibrium model of low aspect-ratio toroidal plasma with energetic beam ions *Phys. Plasmas* **10** 3240–51

[34] Carlsson J. 2001 Breakdown of adiabatic invariance in spherical tokamaks *Phys. Plasmas.* **8** 4725–8

[35] Escande D.F. and Sattin F. 2021 Breakdown of adiabatic invariance of fast ions in spherical tokamaks *Nucl. Fusion* **61** 106025

[36] Cecconello M., Boeglin W., Keeling D., Conroy S., Klimek I. and Perez R.V. 2018 Discrepancy between estimated and measured fusion product rates on MAST using TRANSP/NUBEAM *Nucl. Fusion* **59** 016006

[37] Sauter O. and Medvedev S.Y. 2013 Tokamak coordinate conventions: *COCOS Comput. Phys. Commun.* **184** 293–302

[38] Heidbrink W.W. and Sadler G.J. 1994 The behaviour of fast ions in tokamak experiments *Nucl. Fusion* **34** 535

[39] Breizman B.N. and Sharapov S.E. 1995 Energetic particle drive for toroidicity-induced Alfvén eigenmodes and kinetic toroidicity-induced Alfvén eigenmodes in a low-shear tokamak *Plasma Phys. Control. Fusion.* **37** 1057

[40] Candy J. and Rosenbluth M.N. 1994 Nonideal theory of toroidal Alfvén eigenmodes *Phys. Plasmas.* **1** 356–72

[41] Berk H.L., Van Dam J.W., Guo Z. and Lindberg D.M. 1992 Continuum damping of low-n toroidicity-induced shear Alfvén eigenmodes *Phys. Fluids B* **4** 1806–35

[42] Li M., Breizman B.N., Zheng L.J. and Chen E.Y. 2015 Continuum absorption in the vicinity of the toroidicity-induced Alfvén gap *New J. Phys.* **17** 125001

[43] Rosenbluth M.N., Berk H.L., Van Dam J.W. and Lindberg D.M. 1992 Mode structure and continuum damping of high-n toroidal Alfvén eigenmodes *Phys. Fluids B* **4** 2189–202

[44] Ryan D.A., Martin R., Appel L., Ayed N.B., Kogan L. and Kirk A. 2023 Initial progress of the magnetic diagnostics of the MAST-U tokamak *Rev. Sci. Inst.* **94** 073501

[45] Fitzgerald M. and Breizman B.N. 2025 Solution of the linear wave-particle kinetic equation for global modes of arbitrary frequency in a tokamak *Fund. Plasma Phys.* **13** 100084

[46] Todo Y. 2018 Introduction to the interaction between energetic particles and Alfven eigenmodes in toroidal plasmas *Rev. Modern Plasma Phys.* **3** 1

[47] Todo Y., Berk H.L. and Breizman B.N. 2010 Nonlinear magnetohydrodynamic effects on Alfvén eigenmode evolution and zonal flow generation *Nucl. Fusion* **50** 084016

[48] Todo Y., Berk H.L. and Breizman B.N. 2012 Simulation of Alfvén eigenmode bursts using a hybrid code for nonlinear magnetohydrodynamics and energetic particles *Nucl. Fusion* **52** 033003